國立臺灣大學工學院材料科學與工程學系

碩士論文

Department of Materials Science and Engineering

College of Engineering

National Taiwan University

Master's Thesis

時效處理對預應變 Al-Cu-Li 合金的影響及 T_1 析出物的原子尺度研究

Effect of Aging Treatments on Pre-Strain Al-Cu-Li Alloy and Atomic-Scale Investigation of T_1 Precipitates

林泓任

Hung-Jen Lin

指導教授：楊哲人 博士

Advisor: Jer-Ren Yang, Ph.D.

中華民國 113 年 7 月

July, 2024

doi:10.6342/NTU202402902

國立臺灣大學碩士學位論文
口試委員會審定書
MASTER'S THESIS ACCEPTANCE CERTIFICATE
NATIONAL TAIWAN UNIVERSITY

（論文中文題目）
(Chinese title of Master's Thesis)

時效處理對預應變 Al-Cu-Li 合金的影響及 T_1 析出物的原子尺度研究

（論文英文題目）
(English title of Master's Thesis)

Effect of Aging Treatments on Pre-Strain Al-Cu-Li Alloy and Atomic-Scale Investigation of T_1 Precipitates

本論文係 **林泓任** (R11527058) 在國立臺灣大學材料科學與工程學系、所完成之碩士學位論文，於民國 113 年 7 月 29 日承下列考試委員審查通過及口試及格，特此證明。

The undersigned, appointed by the Department / Graduate Institute of Material Science and Engineering on 29th/July/2024 have examined a Master's Thesis entitled above presented by **Lin, Hung-Jen** (R11527058) candidate and hereby certify that it is worthy of acceptance.

口試委員
Oral examination committee:

楊哲人 楊哲人
（指導教授 Advisor）

鍾采甫 鍾采甫

王涵聖 王涵聖

陳志遠 陳志遠

蕭健男 蕭健男

系（所、學位學程）主管 Director：蔡豐羽 蔡豐羽

誌謝

能夠在這裡寫下這篇致謝，首先我要感謝兩年前考上研究所後，楊哲人老師願意讓我加入 PT Group。在這裡，我學到了很多寶貴的知識，老師在會議中的指導對我的人生有著深遠的影響。

我要特別感謝口試委員。鍾采甫老師給予我關於 review paper 的寶貴建議，王涵聖經理對我爆炸試片的濃厚興趣，陳志遠教授對我論文格式的指導，以及蕭健男博士在實驗設計上的建議。感謝各位的寶貴指教。

感謝 PT Group 的各位同仁。首先我要排除 Leo，因為他偷吃了我的奶油餅，我至今還記得。感謝博士班的學長姐們，曹博、仕淵、家俊、+0、千育，每次我請教你們實驗問題時，你們的回答總是像在處理自己的實驗，真的是超級感謝。還有碩士班的學長姐，芊瑜、駱哥、宜嫻、冠名、廷融，感謝你們教我 TEM、SEM 以及德州撲克。感謝同屆的同學們，柴犬帕奇 AKA 書誠、雨蓁、詩雅，我們一起度過了許多艱難的時光，做實驗時的聊天讓我堅持了下來。感謝學弟妹們 Cody、巨人、昱安、子柔、子恩、勇安，感謝你們在實驗室的幫助。

感謝在台積電實習時教我 TEM 知識的學長姐們，你們對這篇論文也有很大的幫助，超級感謝。感謝北科大幫我做 CAF 的嘉宏老哥，你的幫忙讓我受益匪淺，希望你也能順利畢業。感謝陳先生和柏翰學長，維持 TEM 在良好狀態的工作。感謝林師傅切割的試片，更要感謝材料系辦的支持。感謝 HC LAB 的各位，讓我在實驗無聊時有伴可聊。感謝系排的各位，謝謝健工健康廠的夥伴們，讓我保持健康

doi:10.6342/NTU202402902

的身體，也一起參加了許多比賽。特別感謝 Sam，你開發的 GPT 太強了，還有 David Goggins，whose gonna carry the boat or logs。

感謝 PJ 鼓勵我考研究所，否則也不會有這篇論文。感謝我的朋友們，在我需要的時候總是出現。

最後，最重要的是感謝我的家人們，感謝你們把我養大，並提供資金讓我繼續學業，你們是這本論文的最大貢獻者。

還有我自己，林泓任，你做得不錯，終於完成了論文。雖然過程中沒有特別努力，但結果很不錯。祝你在台積電的日子裡依然開心，希望你成為台積電最健康的人。

可能還有一些人沒有提到，但我心中充滿感恩，愛你們。

doi:10.6342/NTU202402902

中文摘要

本實驗使用高強度且輕量化的 AA2050 (Al-Cu-Li) 鋁合金，對其施加預應變，使材料內部充滿差排以促使析出物成核，再以不同的時效方法（如人工時效和潛變時效）促使大量奈米析出物 T1 生成，以強化材料基地。隨後測量材料的機械性能，包括硬度及拉伸試驗，並使用穿透式電子顯微鏡（TEM）和小角度 X 光散射（SAXS）分析不同時效階段的析出物形貌，探討材料顯微結構與機械性能之間的關係。

在材料預應變後，利用明場像及高角度環形暗場影像（HAADF）技術，觀察到 T_1 析出物在差排、二次相邊界及晶界上的異質成核。發現基地中的差排和二次相邊界上析出許多單層 T_1，而晶界上則出現特殊的八層粗大 T_1 析出物。這樣的晶界偏析也會造成析出空乏區。使用潛變時效能減少析出空乏區的大小，進而減少其帶來的負面影響。相比人工時效，潛變時效不僅可以提高材料的降伏強度（增加 21MPa），還能提高材料的延展性，提供了一種有效的方法。

由於雙球差穿透式電子顯微鏡 Spectra 300 的引入，能夠深入了解析出物的原子尺度結構，本文還分析了 T_1 的前驅物 GP(T_1)及 T1 之間的差異與它們的 in-situ 轉變機制，並發現 T_1 在兩種增厚機制互相糾結的特殊現象。此外，拍攝了拉伸試驗後的試片，展示了在不同晶帶軸下 T_1 析出物被差排切過的影像。最後，通過積分差分相位對比（iDPC）技術，首次實現了 T_1 析出物中鋰原子的直接成像，為深入解析析出物的各項機制提供了新的研究方法。

關鍵字: AA2050 (Al-Cu-Li) 鋁合金; 穿透式電子顯微鏡; T_1 析出物; 積分差分相位對比; 時效處理

doi:10.6342/NTU202402902

ABSTRACT

This study utilizes the high-strength and lightweight AA2050 (Al-Cu-Li) aluminum alloy, which is pre-strain to introduce dislocations within the material, facilitating the nucleation of precipitates. Subsequent aging treatments, such as artificial aging and creep aging, are applied to generate a significant amount of nano-scale T_1 precipitates, thereby strengthening the matrix. The mechanical properties, including hardness and tensile tests, are then measured. Additionally, transmission electron microscopy (TEM) and small-angle X-ray scattering (SAXS) are used to analyze the morphology of the precipitates at different aging stages, exploring the relationship between the microstructure and mechanical properties of the material.

After pre-strain, bright-field (BF) and high-angle annular dark-field (HAADF) imaging techniques reveal the heterogeneous nucleation of T_1 precipitates at dislocations, second-phase boundaries, and grain boundaries. Numerous single-layer T_1 precipitates are observed at dislocations and second-phase boundaries, while unique eight-layer thick T_1 precipitates appear at grain boundaries. This elemental segregation at grain boundaries also results in precipitate-free zones. Creep aging reduces the size of these precipitate-free zones, thereby decreasing their adverse effects. Compared to artificial aging, creep aging not only increases the yield strength of the material (by 21 MPa) but also enhances its ductility, providing an effective treatment method.

doi:10.6342/NTU202402902

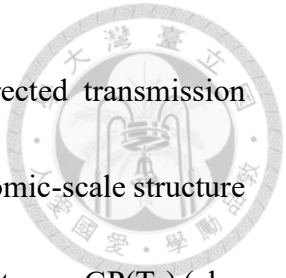

With the introduction of the double spherical aberration-corrected transmission electron microscope Spectra 300, an in-depth understanding of the atomic-scale structure of precipitates is achieved. This study also examines the differences between GP(T_1) (also known as T_1^p) and T_1, along with their in-situ transformation mechanisms, revealing a unique phenomenon where T_1 thickening mechanisms are intertwined. Additionally, post-tensile test samples are imaged, showing dislocation shearing of T_1 precipitates along different crystallographic orientations. Finally, by employing integrated differential phase contrast (iDPC) techniques, the direct imaging of lithium atoms within T_1 precipitates is achieved for the first time, offering a novel method for detailed analysis of precipitate mechanisms.

Keywords: AA2050 (Al-Cu-Li) aluminum alloy; transmission electron microscopy; T_1 precipitates; integrated differential phase contrast; aging treatment

doi:10.6342/NTU202402902

CONTENTS

doi:10.6342/NTU202402902

doi:10.6342/NTU202402902

doi:10.6342/NTU202402902

doi:10.6342/NTU202402902

LIST OF FIGURES

doi:10.6342/NTU202402902

doi:10.6342/NTU202402902

doi:10.6342/NTU202402902

doi:10.6342/NTU202402902

doi:10.6342/NTU202402902

LIST OF TABLES

doi:10.6342/NTU202402902

Chapter 1 Introduction

Aluminum alloys are widely utilized in the aerospace and automotive industries due to their high strength-to-weight ratio and excellent corrosion resistance. These light metals are crucial in these sectors because their lower density significantly reduces energy consumption during vehicle operation. This aligns with global trends towards low-carbon and environmentally friendly technologies. Among aluminum alloys, Al-Cu-Li alloys are particularly notable for their low density, offering substantial energy savings if widely adopted.

Formability and strength are the most critical properties of aluminum alloys. It is essential to shape aluminum alloys into various components while maintaining their mechanical strength to meet the rigorous demands of aerospace applications. Creep-age forming, a method that simultaneously enhances strength and formability, has attracted significant attention in the industry. Therefore, this research will discuss the differences brought about by traditional artificial aging and creep-aging from both microstructural and mechanical performance perspectives in pre-strain aluminum alloys.

The primary precipitate strengthening phase in Al-Cu-Li alloys, T_1, is also of significant interest. Understanding the phase transformation, growth, and strengthening mechanisms of T_1 precipitates is essential for the further development of these alloys. The recent introduction of the advanced TEM instrument, the dual-spherical aberration-

doi:10.6342/NTU202402902

corrected TEM Spectra 300 at National Taiwan University, enables us to capture atomic-scale images, facilitating a deeper analysis of these mechanisms.

This thesis comprises seven chapters. Chapter 2 reviews the literature on 2xxx series aluminum alloys and the impacts of processing changes. Chapter 3 provides a detailed explanation of the experimental procedures and equipment used, along with the methods for specimen preparation. Chapter 4 discusses the effects of different aging treatments on the material's mechanical properties and microstructure. Chapter 5 delves into atomic-scale mechanisms of precipitates. Finally, Chapter 6 presents a general conclusion summarizing all results, and Chapter 7 outlines future work.

doi:10.6342/NTU202402902

Chapter 2 Literature Review

2.1 2xxx Series Aluminum Alloys

In this section, we will discuss various series of aluminum alloys and common heat treatments. Following this, we will delve into the effects of alloying elements on 2xxx series aluminum alloys and provide a detailed introduction to all precipitates in the 2xxx series. Finally, we will describe in detail the phase transformation mechanism, growth, and strain hardening mechanisms of the primary precipitate phase, T_1.

2.1.1 Introduction of Aluminum Alloys

Aluminum, the most abundant metal in the Earth's crust, is also the third most abundant element overall. It constitutes approximately 8.2% by weight of the Earth's solid surface [1, 2], featuring properties such as easy machinability, high strength-to-weight ratio, light weight, ductility, and excellent thermal conductivity [3]. Owing to these attributes, aluminum is extensively used in the automotive and aerospace industries. It is the most widely utilized non-ferrous metal.

However, the strength of pure aluminum is relatively low [4]. To meet the demands of various applications, alloying elements such as Cu, Mg, Mn, and Si are added to aluminum. Additionally, processes like age hardening and strain hardening are employed to enhance its strength. Since 1945, the Aluminum Association of the United States has

doi:10.6342/NTU202402902

classified aluminum alloys based on the elements added. As shown in Table 2-1, these alloys are divided into eight major categories. The naming convention starts with 'AA' followed by a four-digit number. Specifically, the 2xxx, 6xxx, and 7xxx series are heat-treatable, while the 1xxx, 3xxx, 4xxx, and 5xxx series are mechanically workable [5].

Table 2-1 Aluminum alloy series and their properties and applications [5-9]

Series	**Main alloying element**	**Properties**	**Applications**
1xxx	Al > 98.8wt%	Excellent corrosion resistance, workability, electrical and thermal conductivity.	Electrical applications
2xxx	Cu	High strength and toughness, good fatigue resistance.	Airframes, skin of aircrafts, rocket chamber.
3xxx	Mn	Good workability combined with moderate strength.	Cooking utensils, aluminum beverage cans
4xxx	Si	Sufficient quantities of silicon reduce the melting point of aluminum.	Filler materials for welding 6xxx series alloys
5xxx	Mg	High strength, excellent corrosion resistance.	Pressure vessels, storage tanks, construction applications
6xxx	Mg and Si	High strength, good weldability, and excellent corrosion resistance.	Phone case, aircraft constructions, automotive industries
7xxx	Zn	Very high strength and good fracture toughness.	Aircraft, automotive applications, military applications
8xxx	Other elements	-	-

doi:10.6342/NTU202402902

In 1905, German scientist Alfred Wilm conducted hardness tests on a quenched Al-Cu alloy. An unexpected delay over the weekend led to increased hardness by Monday, resulting in the discovery of age hardening. This breakthrough marked the beginning of what could be called the 'age of age hardening', stimulating subsequent research into various aging processes. The Aluminum Association established a temper designation system for different heat treatments, presented with a hyphen between the alloy and temper designations (e.g., AA2050-T8) [10], as shown in Table 2-2.

Table 2-2 Aluminum temper designations and their descriptions[10, 11]

Temper	**Description**
F	As fabricated
O	Annealed
H	Strain hardened
T1	Cooled from elevated temperature shaping process and naturally aged to a substantially stable condition
T2	Cooled from an elevated temperature shaping process, cold worked, and naturally aged to a substantially stable condition
T3	Solution heat treated, cold worked, and naturally aged to a substantially stable condition
T4	Solution heat treated and naturally aged to a substantially stable condition
T5	Cooled from an elevated temperature shaping process, then artificially aged
T6	Solution treated, then artificially aged
T7	Solution heat treated and overaged/stabilized
T8	Solution heat treated, cold worked, then artificially aged
T9	Solution heat treated, artificially aged, then cold worked
T10	Cooled from an elevated temperature shaping process, cold worked, then artificially aged

doi:10.6342/NTU202402902

2.1.2 Effects of Solute Element Addition

Years after Wilm's discovery of age hardening, Starke and Hornbogen clarified that this mechanism results from precipitation from a supersaturated solid solution. They observed that elements in a supersaturated solution within aluminum alloys could precipitate into tiny particles within the matrix at low temperatures [12]. Consequently, scientists began experimenting with the addition of various elements to aluminum alloys. Among these, lithium garnered attention due to its high solubility in aluminum at high temperatures, and as the lightest metal, it further contributed to the light-weighting of materials.

Today, the development of aluminum-lithium (Al-Li) alloys is typically categorized into three generations. The origin of the first generation dates back to 1945 when I.M. LeBaron patented an Al-Cu-Li-Mn-Cd alloy, around the same time Hardy and Silcock were investigating the phase diagram and tensile properties of similar alloys [13]. This era marked the initial interest in the applications of Al-Li alloys. Concurrently, the introduction of AA7075 (Al-Zn-Mg-Cu) by Alcoa, which provided superior strength and toughness compared to Al-Li alloys, significantly influenced the market. Additionally, the early Al-Li alloys were phased out from their use in the Navy RA-5C Vigilante aircraft due to their low fracture toughness, poor ductility, and the high reactivity of lithium, which complicated the melting process [14]. These factors led to the discontinuation of

doi:10.6342/NTU202402902

the first generation Al-Li alloys, as they lacked broad application value.

The second generation of Al-Li alloys saw improvements due to advancements in manufacturing techniques and composition adjustments, resulting in better overall performance than the first generation and beginning to be used in some secondary structures on aircraft. However, issues with ductility and fracture toughness still needed improvement. The development of the third generation of Al-Li alloys occurred in the late 1980s when Lockheed Martin Corporation began designing a weldable aluminum base alloy with low density and favorable mechanical properties for use in aerospace launch vehicles and cryogenic tankage. They improved the alloy composition based on AA2219, reducing the lithium content to minimize the formation of the detrimental δ' phase and added silver and magnesium to promote the nucleation of strengthening T_1 precipitates, with zirconium added to control grain size. This alloy, named Weldalite, has a composition of Al-6.3Cu-1.3Li-0.4Ag-0.4Mg-0.14Zr-0.06Fe-0.03Si (wt%) [15], and reportedly achieves a yield strength of 700 MPa. Subsequent scientists used Weldalite as a basis for further adjustments, developing a series of third-generation aluminum-lithium alloys that have been widely applied in the aerospace sector, as detailed in Table 2-3, thereby cementing the success of the third generation of aluminum alloys.

doi:10.6342/NTU202402902

Table 2-3 Chemical composition of some third generation Al-Li alloys (wt%) [12, 16]

Alloy	Li	Cu	Mg	Ag	Zr	Mn	Zn
2195	1.0	4.0	0.4	0.4	0.11		
2196	1.75	2.9	0.5	0.4	0.11	0.35	0.35
2297	1.4	2.8	0.25		0.11	0.3	0.5
2397	1.4	2.8	0.25		0.11	0.3	0.1
2198	1.0	3.2	0.5	0.4	0.11	0.5	0.35
2099	1.8	2.7	0.3		0.09	0.3	0.7
2199	1.6	2.6	0.2		0.09	0.3	0.6
2050	1.0	3.6	0.4	0.4	0.11	0.35	0.25
2060	0.75	3.95	0.85	0.25	0.11	0.3	0.4
2055	1.15	3.7	0.4	0.4	0.11	0.3	0.5

In these third generation Al-Li alloys, the addition of Cu and Li is aimed at precipitating the primary strengthening phase T_1. Varying Cu/Li ratios influence the precipitation sequence differently. When the Cu/Li ratio is 0.5 and 1, the peak-aged alloys tend to precipitate a higher amount of the detrimental δ′ phase [17, 18], leading to poorer fracture toughness. As shown in Table 2-3, the Cu/Li ratio in third-generation aluminum alloys is approximately 2.5. Moreover, the amount of Li added is crucial. The density of aluminum is reduced by about 3% for each weight percent addition of lithium, while Young's modulus is increased by about 6% [19], as illustrated in Figure 2-1. However, an excessive addition of Li tends to facilitate the precipitation of the δ′ phase, which is why third-generation Al-Li alloys tend to have a reduced Li content (less than 1.8%).

doi:10.6342/NTU202402902

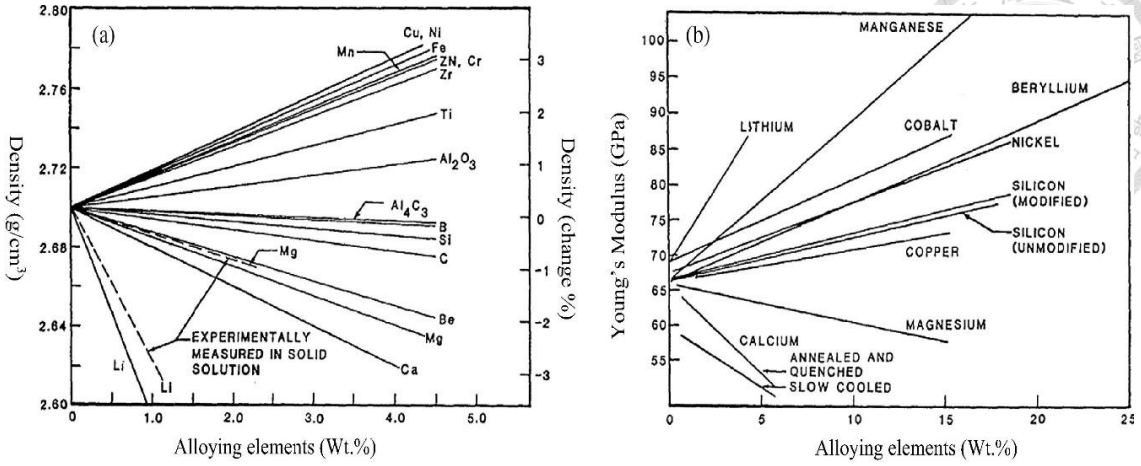

Figure 2-1 Effect of alloying elements on the (a) density and (b) elastic modulus of Al alloys [19].

Apart from the primary additions of Cu and Li, the presence of trace elements also significantly impacts the precipitate phases and grain size. For instance, the addition of Mg has a pronounced effect on the precipitation and strengthening behavior of Al-Cu-Li alloys. Numerous studies indicate that Mg promotes the formation of GP zones and subsequent generation of the T_1 phase. Furthermore, the T_1 phase precipitates with a finer distribution in the presence of Mg [20]. Another study demonstrated that Mg alters the precipitation sequence to predominantly form the T_1 phase, as opposed to mainly θ′ in Mg-free alloys [21].

When Ag, Zn, or their combination is added to Al-Cu-Li-Mg alloys, these elements enhance the precipitation kinetics, increase the volume fraction of precipitates under isothermal conditions, and contribute to higher strength. The presence of Ag at the T_1/matrix interface and Zn within the precipitate seems to play a role in favoring the nucleation of this phase and assists in achieving a higher volume fraction [21].

doi:10.6342/NTU202402902

The addition of Mn results in the formation of $Al_{20}Mn_3Cu_2$ dispersoids, which lead to a finer grain size compared to alloys without Mn [22]. Lastly, the inclusion of Zr, commonly seen in many aluminum alloys, promotes the formation of Al_3Zr dispersoids, controls the recrystallization effects of the material [23], and inhibits the coarsening of the δ′ phase during high-temperature aging.

2.1.3 Types and Characteristics of Precipitates

As mentioned earlier, aluminum alloys are categorized into two types: mechanically workable and heat-treatable. The latter, which includes the 2xxx series aluminum alloys discussed in this thesis, enhances mechanical properties through a precipitation strengthening mechanism. 2xxx series alloys exhibit a variety of precipitates including GP zones, T_1, θ′, S, and δ′. This section will explain the crystal structures and orientation relationships of these precipitates.

- **GP zones**

In 1938, scientists Guinier [24] and Preston [25], through X-ray experiments, discovered that during the early stages of age hardening of Al-Cu alloys, many Cu atoms segregated on the {100} planes of the aluminum matrix. From this discovery, the ordered atomic clusters within the alloy have been termed GP zones.

Subsequent research continued to explore the structure and morphology of GP zones.

doi:10.6342/NTU202402902

By 1958, the first Transmission Electron Microscopy (TEM) images of GP zones in Al-Cu alloys were captured [26], as shown in Figure 2-2, revealing edge-on configurations with a thickness of 3-4Å and a diameter of 80Å.

With the advancement of TEM technology, High-Resolution Transmission Electron Microscopy (HRTEM) identified two types of GP zones in Al-Cu alloys, as shown in Figure 2-3: the GPI zone consisting of a single layer of Cu atoms, and the GP II zone, which features a double layer of Cu atoms structure [27]. This research has led to a clear understanding of GP zones in Al-Cu systems

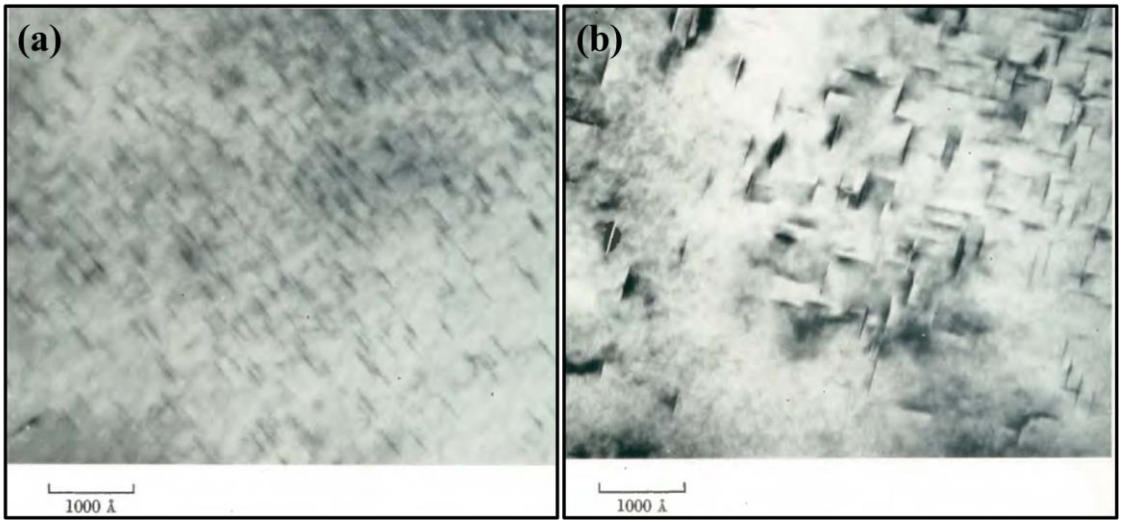

Figure 2-2 The TEM images of GP zones under $[001]_{Al}$ zone axis [26].

doi:10.6342/NTU202402902

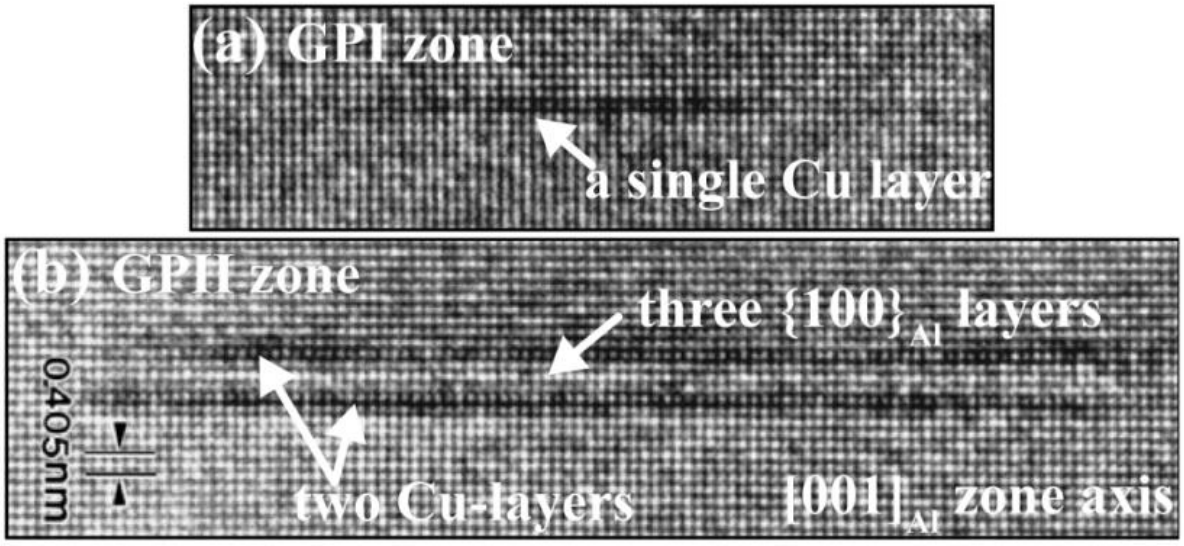

Figure 2-3 The HRTEM images of (a) GPI zone and (b) GPII zone under $[001]_{Al}$ zone axis [27, 28]

In the case of Al-Cu-Li-Mg alloys, there are generally believed to be three types of GP zones [29], each located on different habit planes: GP(T_1) zones on the $\{111\}_{Al}$ plane [30], GP(θ″) zones on the $\{100\}_{Al}$ plane [31], GPB zones on the $\{120\}_{Al}$ plane [31]. Observed under the $[110]_{Al}$ zone axis, Figure 2-4a reveals two edge-on configurations of GP(T_f) on their respective habit planes, considered precursors to T_1 precipitates. Figure 2-4b, as shown via HR-STEM images, displays a single layer of Cu atoms in GP(θ″) on the (020) habit plane, similar to the GPI zone in the Al-Cu system, which evolves into θ′ during subsequent heat treatments. Figure 2-4c illustrates the GPB zone as an ordered aggregation of Cu and Mg on the $(2\bar{4}0)$ habit plane, believed to develop into S precipitates during further processing.

doi:10.6342/NTU202402902

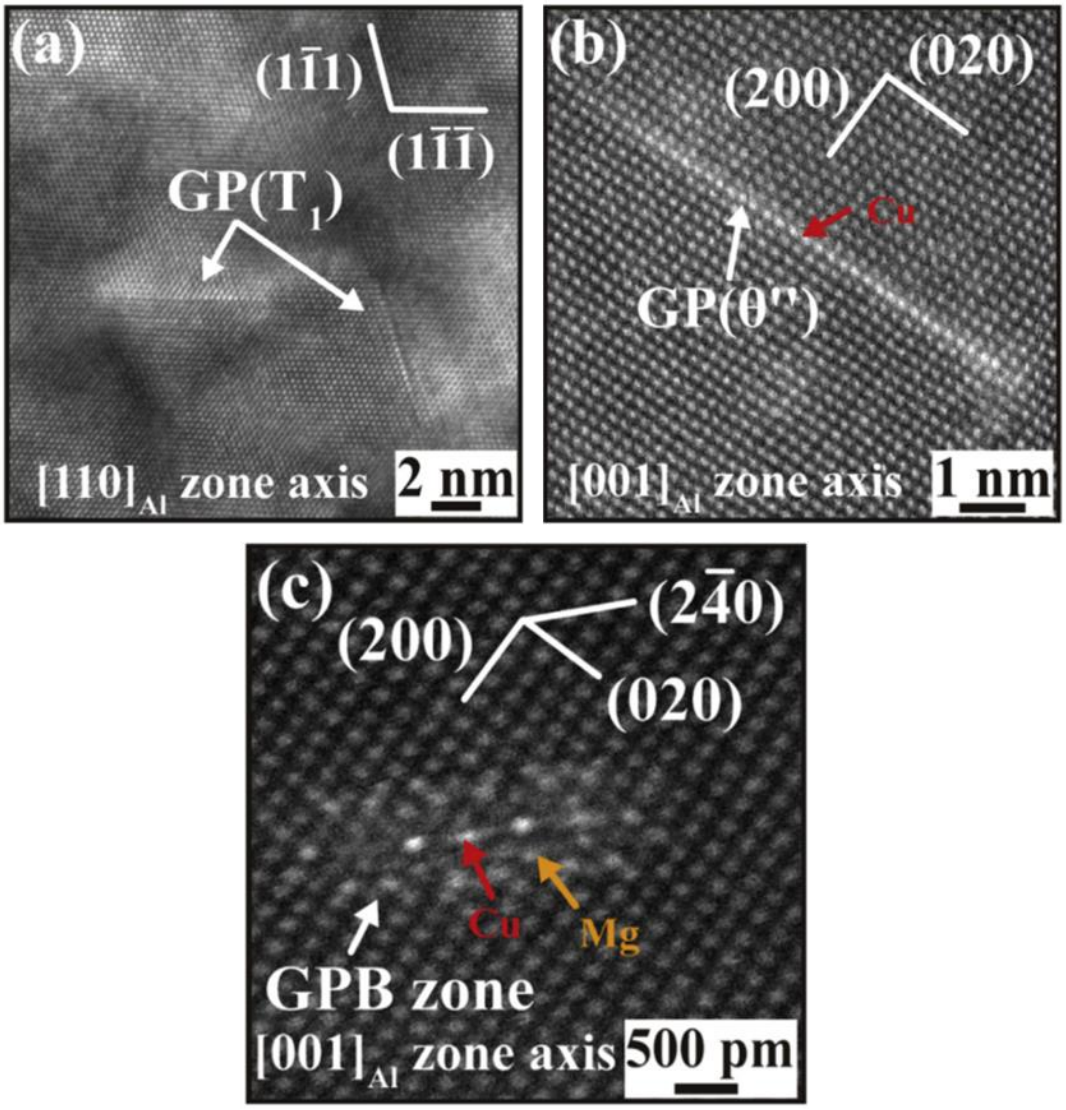

Figure 2-4 (a) HR-TEM image illustrating two GP(T_1) zones in edge-on configurations. (b) HR-STEM image showing a GP(θ″) zone. (c) HR-STEM image showing a GPB zone composed of Cu and Mg atoms [29]

- **T_1 phase**

The T_1 phase is the primary strengthening precipitate phase in most Al-Cu-Li alloys [32]. Although it is commonly referred to as Al_2CuLi, studies indicate that the T_1 phase does not exactly correspond to the Al_2CuLi composition. However, for simplicity, it is often denoted as Al_2CuLi. Within the aluminum matrix, T_1 manifests as a plate-like

doi:10.6342/NTU202402902

precipitate with a high aspect ratio. The thickness of these precipitates is approximately 1.3 nm, which is about the thickness of five layers of the close-packed {111} planes of aluminum. The length of these precipitates can reach up to 200 nm or more during peak aging. This phase is hexagonal, characterized by a space group P6/mmm with lattice parameters a = 0.496 nm c = 0.935 nm.

Historically, five significant crystallographic models of the T_1 precipitate have been proposed [33-37], as illustrated in Figure 2-5. These models are divided into two categories. The first category, proposed by J.C. Huang in 1987 [33] and later modified by J.M. Howe and others in 1988 [34], is based on the stacking of four hexagonal layers similar to the {111} planes of the Al matrix, with each layer having a width of 0.233 nm. The second model, introduced by Van Smaalen in 1990 using single-crystal X-ray diffraction [35], argues that the T_1 structure does not consist merely of a stacking of four hexagonal layers but rather features several corrugated Al-Li layers. These two model types have been the subject of ongoing debate until 2011 when Donnadieu and Dwyer [36, 37], using advanced TEM techniques, confirmed that the T_1 precipitates more closely resemble the model proposed by Van Smaalen. However, due to the invisibility of Li elements in standard Z-contrast images, some adjustments to this model are still warranted.

doi:10.6342/NTU202402902

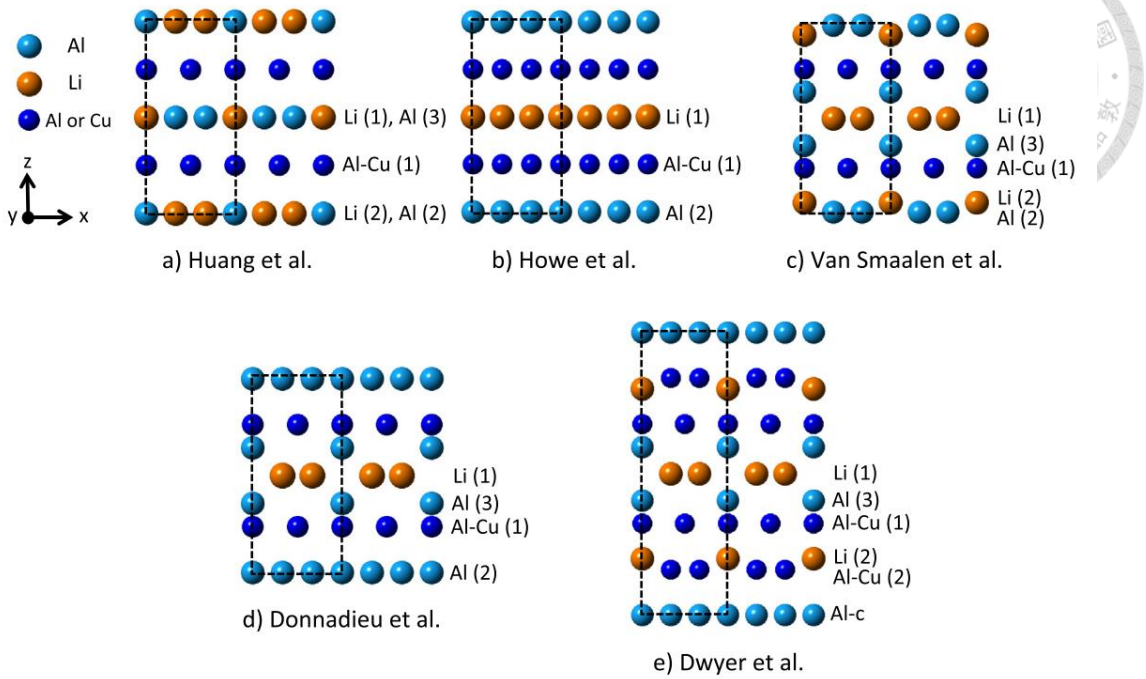

Figure 2-5 Atomic models for T_1 phase. The structures are shown along $[11\bar{2}0]$ direction (y-axis). The z-axis represents [0001], which corresponds to the normal direction of {111} Al plane [38]

In 2018, Kyoungdoc Kim employed density functional theory (DFT) calculations to analyze the structure and composition of the T_1 phase by comparing the energetic stability of the five previously proposed models [38]. He proposed a more energetically stable crystal structure, $Al_6Cu_4Li_3$, as shown in Figure 2-6 and Figure 2-7. By 2021, this model was refined to also achieve thermodynamic stability even at 600K [39], making it the most widely accepted model for the T_1 phase today.

doi:10.6342/NTU202402902

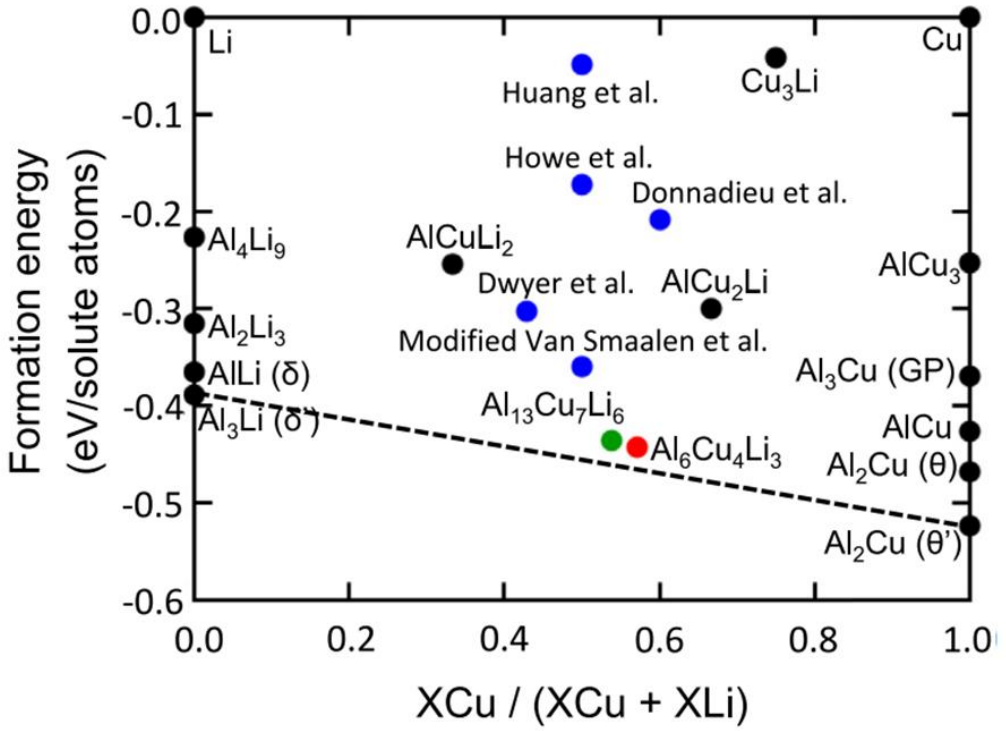

Figure 2-6 Calculated formation energies (eV/solute atom). These energies represent the thermodynamic stability of various compounds when in equilibrium with Al matrix [38]

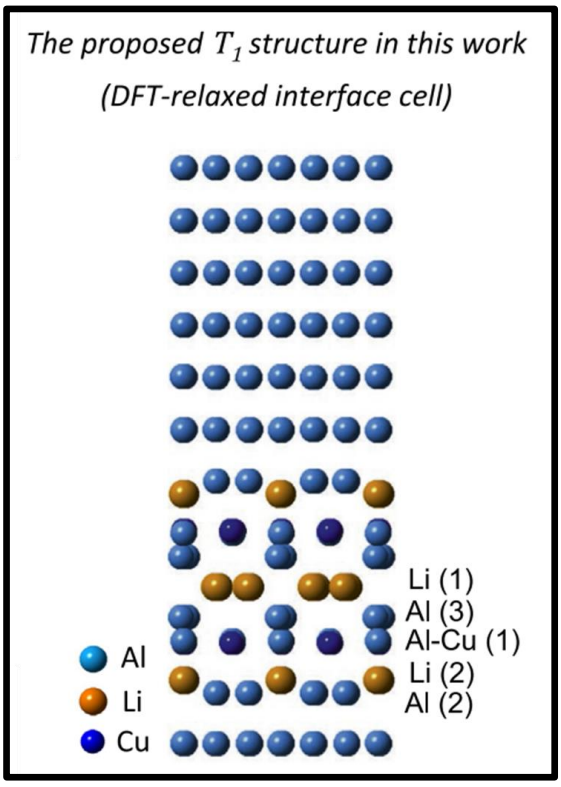

Figure 2-7 Relaxed supercells of the ground-state structure ($Al_6Cu_4Li_3$) [38]

doi:10.6342/NTU202402902

It is important to note that the high aspect ratio, plate-like T_1 precipitates exhibit four variants, as indicated in Table 2-4. The orientation relationship of these variants necessitates specific zone axes for observation in TEM to view the precipitates in an edge-on configuration. Non-edge-on precipitates are challenging to observe due to strong matrix contrast. For instance, from the [110] Al zone axis, edge-on needle-like $T_1^{(2)}$ and $T_1^{(4)}$ can be observed, while $T_1^{(1)}$ and $T_1^{(3)}$ remain undetectable, as shown in Figure 2-8.

Table 2-4 Orientation relationship of T_1 precipitates

T_1	**Orientation Relationship**	
1	$(0001)_{T1}//(111)_{Al}$	$[10\bar{1}0]_{T1}//[\bar{1}10]_{Al}$
2	$(0001)_{T1}//(1\bar{1}1)_{Al}$	$[10\bar{1}0]_{T1}//[110]_{Al}$
3	$(0001)_{T1}//(11\bar{1})_{Al}$	$[10\bar{1}0]_{T1}//[\bar{1}10]_{Al}$
4	$(0001)_{T1}//(1\bar{1}\bar{1})_{Al}$	$[10\bar{1}0]_{T1}//[110]_{Al}$

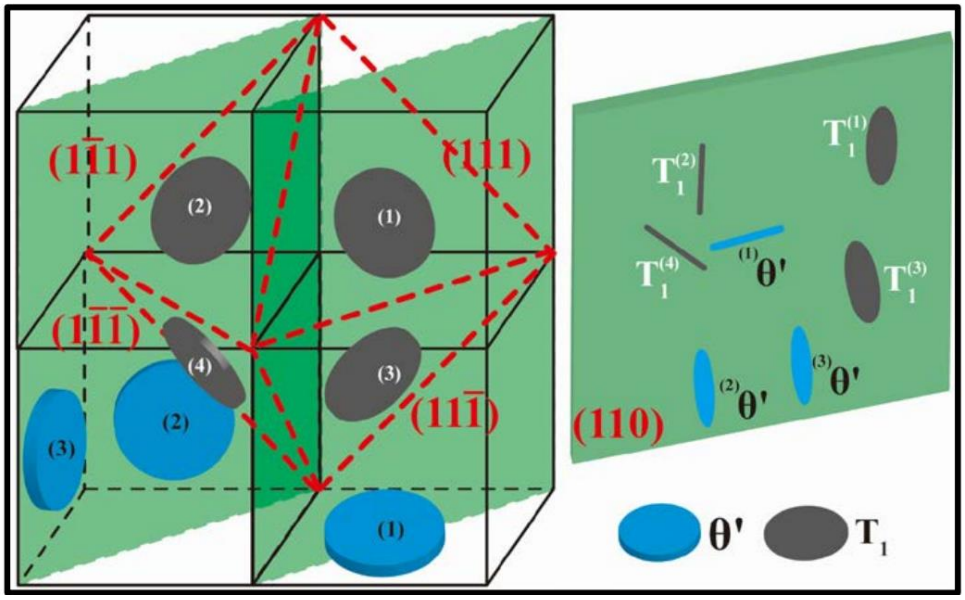

Figure 2-8 Schematic diagram of the orientation relationships of T_1 and θ′ precipitates, with T_1 indicated in black and θ′ in blue [29]

doi:10.6342/NTU202402902

- **θ′ phase**

θ′ precipitates serve as the secondary strengthening phase in Al-Cu-Li alloys. The crystal structure of θ′ is body-centered tetragonal (space group I4/m), with lattice constants a = 4.04Å and c =5.80Å [40]. The nominal stoichiometry is Al2Cu. Similar to T_1, θ′ also forms as a plate-like precipitate with a high aspect ratio. The variants and orientation relationships of θ′ precipitates are detailed in Table 2-5.

θ′ precipitates exhibit three variants on the {001} habit plane. To observe θ′ precipitates, one can use either the [001] or [110] zone axes. The former allows for the observation of two edge-on configurations, as illustrated in Figure 2-9, while the latter permits observation of only one configuration.

Table 2-5 Orientation relationship of θ′ precipitates

θ′	**Orientation Relationship**	
1	$(001)_{\theta'}//(001)_{Al}$	$[100]_{\theta'}//[100]_{Al}$
2	$(010)_{\theta'}//(001)_{Al}$	$[100]_{\theta'}//[100]_{Al}$
3	$(100)_{\theta'}//(001)_{Al}$	$[010]_{\theta'}//[010]_{Al}$

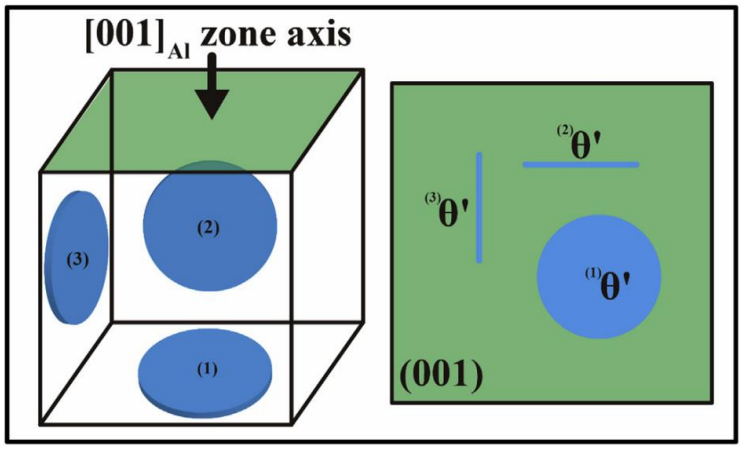

Figure 2-9 Schematic diagram of the orientation relationships of θ′ precipitates [29]

doi:10.6342/NTU202402902

- **δ′ phase**

The δ′ (Al_3Li) phase exhibits a typical face-centered cubic (FCC) superlattice structure and is completely coherent with the matrix. In Al-Cu-Li alloys, the δ′ phase precipitates in two distinct manners. One form is the precipitation of spherical δ′ particles. The other involves nucleation adjacent to GP(θ″) zone and θ′ precipitates, gradually evolving into δ′/GP(θ″)/δ′ and δ′/θ′/δ′ sandwich structures [41].

However, the lower shear modulus of the δ′ phase facilitates repeated dislocation slip and shear along the same slip plane. As a result, δ′ exhibits significantly lower strengthening capability compared to the T_1 phase [33, 41]. Consequently, as mentioned in Section 2.1.2, the third generation of Al-Li alloys has reduced lithium content to minimize the precipitation of the δ′ phase.

- **S phase**

The S phase (Al_2CuMg), which evolves from GPB zones, forms as rod-like precipitates with an orthorhombic structure [42]. It possesses 12 variants, and the orientation relationship between the S phase and the matrix is generally expressed as $(001)_S$ // $(2\bar{1}0)_{Al}$, $[100]_S$ // $[001]_{Al}$. When using the $[112]_{Al}$ zone axis to observe T_1 precipitates, it is also possible to simultaneously observe two edge-on S precipitates.

doi:10.6342/NTU202402902

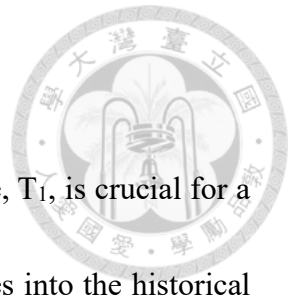

2.1.4 Evolution Mechanism of T_1 Precipitates

Understanding the evolution of the primary strengthening phase, T_1, is crucial for a comprehensive grasp of Al-Cu-Li alloy systems. Section 2.1.3 delves into the historical development of the crystal structures of GP zones and T_1 precipitates. A substantial amount of literature has proposed various models to discuss these structures. However, due to the complexities of in-situ experiments and theoretical challenges, the evolution among these precipitates has been less thoroughly discussed.

Among the notable studies on T_1 evolution, the research by Z. Gao et al. in 2015 stands out [43]. Through HR-STEM image analysis, differences in imaging and structure between GP(T_1) (sometimes referred to as T_1^P) and T_1 were proposed. As shown in Figure 2-10 c and d, the GP(T_1) zone consists of two Cu-rich planes sandwiching a $\{111\}_{Al}$ matrix plane and is fully coherent with the Al matrix, distinct from the arrangement seen in Figure 2-10 a and b, where T_1 features a completely black Li layer. Moreover, Gao et al. established a possible transformation mechanism and supported it with first-principles calculations to demonstrate its theoretical viability. As illustrated in Figure 2-11, the evolution from GP(T_1) to T_1 can be divided into three steps, with each step showing a gradual decrease in the corresponding formation enthalpy, indicating an energetically favorable transformation process.

doi:10.6342/NTU202402902

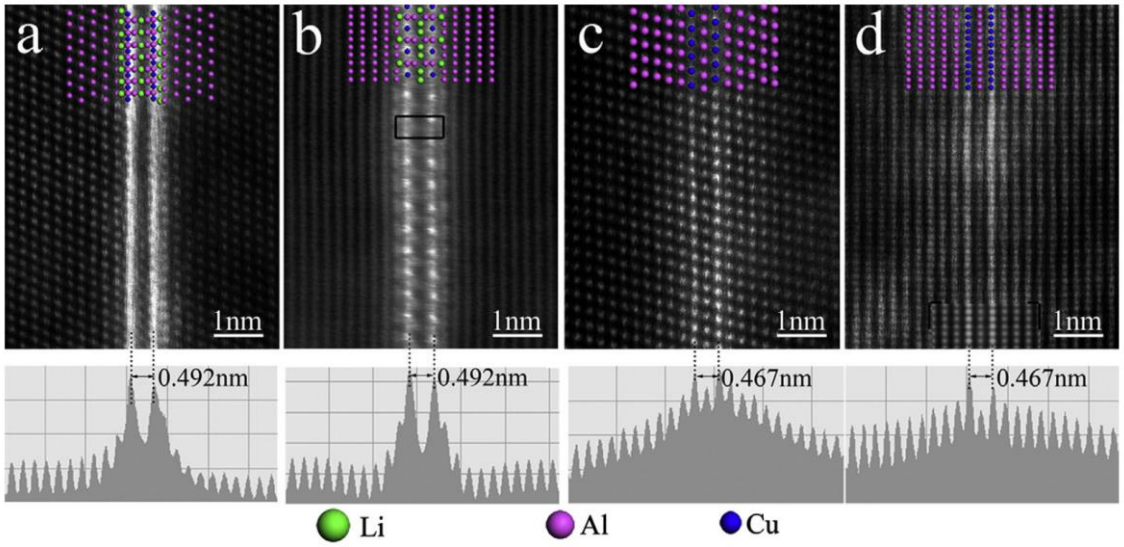

Figure 2-10 HAADF-STEM images of the precipitates: (a) a $[110]_{Al}$ image and (b) a $[112]_{Al}$ image of the T_1 precipitate; (c) a $[110]_{Al}$ image and (d) a $[112]_{Al}$ image of the GP(T_1) zones [43]

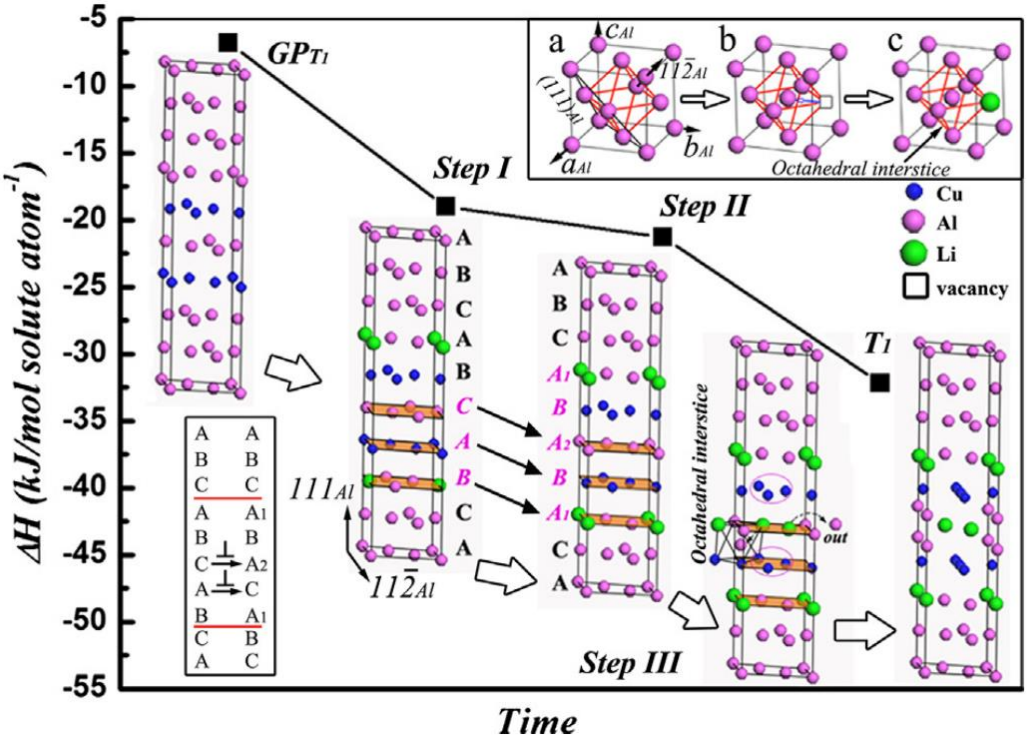

Figure 2-11 The transformation mechanism from the GP(T_1) zone to the T_1 precipitate demonstrated together with the corresponding formation enthalpies ΔH calculated for the illustrated supercells [43]

doi:10.6342/NTU202402902

Two years after the earlier studies, Deng and colleagues captured clearer TEM images and record images showing the in-situ transformation of GP(T_1) to T_1 under different zone axes [30], as depicted in Figure 2-12. Their findings were illustrated in Figure 2-13, which proposed a mechanism for the transformation of GP(T_1) to T_1.

This transformation involves a complex process where the structure transitions from the FCC arrangement of the Al matrix to the hexagonal close-packed (HCP) structure of T_1. The evolutionary process entails not only continued segregation of solute atoms but also a change in the stacking sequence. This change in stacking sequence may be attributed to the successive gliding of a/6⟨112⟩ Shockley partial dislocations on the $\{111\}_{Al}$ planes within the GP(T_1) phase. The passage of the first partial dislocation results in only four layers of HCP stacking. When the second partial dislocation glides on the layer below the previous one, the desired five layers of HCP stacking are obtained. Consequently, the matrix stacking sequence below the T_1 precipitate becomes the BCAB... stacking, as shown in Figure 2-13 c.

These two experiments have significantly clarified the mechanism of T_1 evolution. However, the inability to visualize Li elements in high-angle annular dark-field (HAADF) imaging complicates the research, akin to studying with one eye covered. Therefore, further discussion and investigation into this evolution mechanism are necessary.

doi:10.6342/NTU202402902

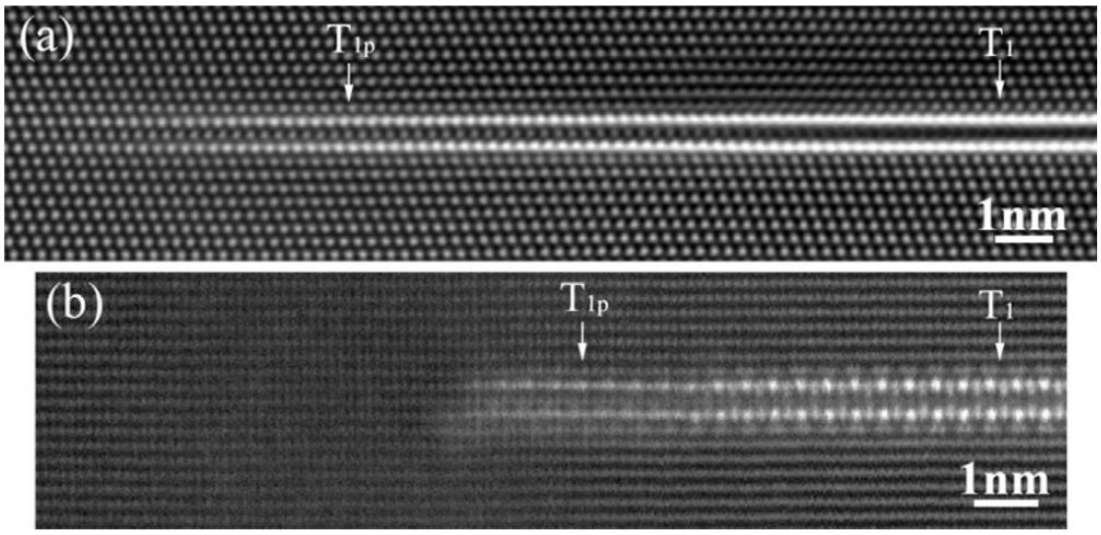

Figure 2-12 HAADF-STEM images of the edge segment of T_1 plates along (a) $[110]_{Al}$ and (b) $[112]_{Al}$ directions. They exhibit the structure transformation from the GP(T_1) (also known as T_1^P) precipitate to the matured T_1 precipitate [30]

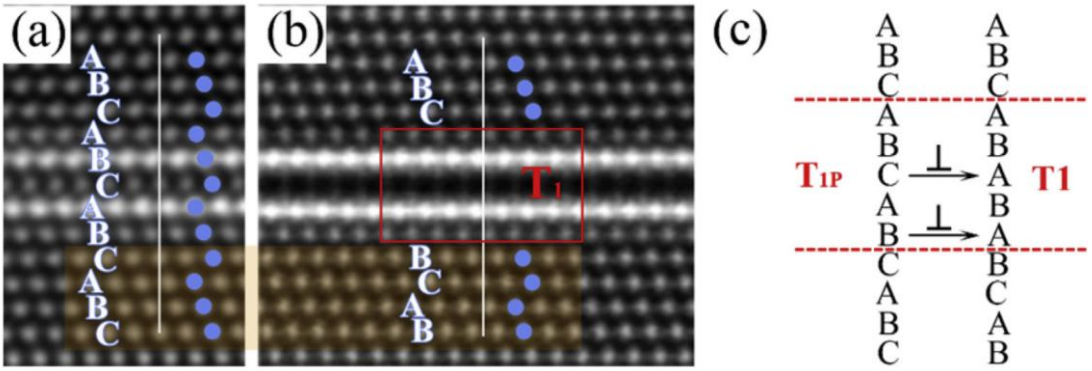

Figure 2-13 HAADF-STEM images of (a) GP(T_1) and (b) T_1 precipitates along the $[110]_{Al}$ directions. The stacking sequence is denoted by A, B and C, and the T_1 precipitate is marked by red rectangle. (c) A schematic illustrates the transformation of stacking sequence from GP(T_1) (also known as T_1^P) phase to T_1 phase [30]

doi:10.6342/NTU202402902

2.1.5 Coarsening Mechanism of T_1 Precipitates

The previous section discussed the mechanism by which GP(T_1) transforms into T_1, which is also relevant for explaining the coarsening mechanism of T_1 precipitates [43, 44], as shown in Figure 2-14, revealing the first type of coarsening mechanism for T_1 precipitates. In Figures Figure 2-14a and b, a GP(T_1) transforms into one-unit-cell-thick T_1 precipitates. With increasing aging time, as illustrated in Figure 2-14c and d, GP(T_1) nucleates on one side of a matured T_1 precipitate. Finally, these metastable precipitates evolve into two-unit-cell-thick T_1 precipitates. We refer to this coarsening process as TYPE-I coarsening.

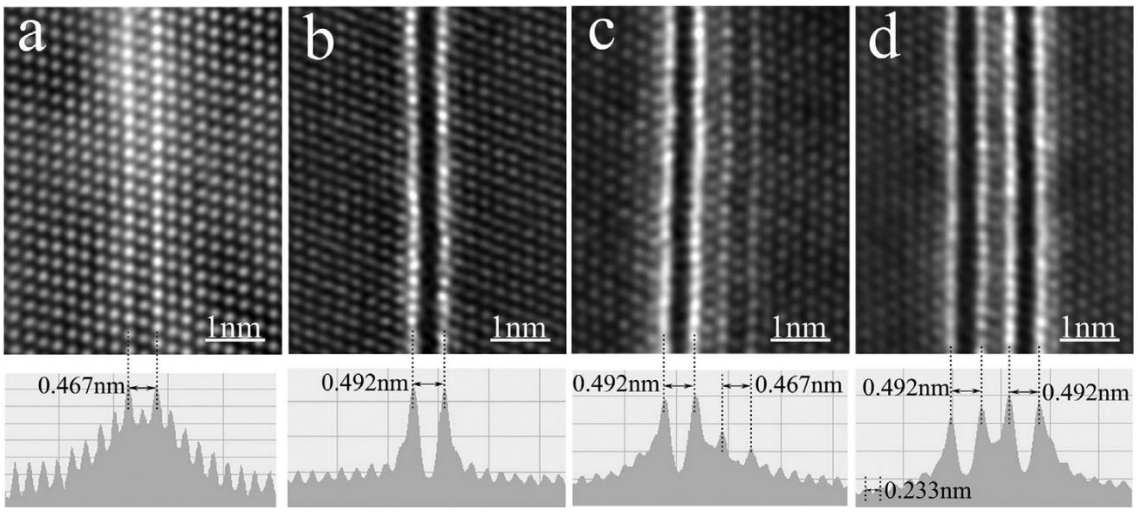

Figure 2-14 HAADF-STEM images revealing the normal growth mechanism of the T_1: (a), the GP(T_1) zone; (b), the matured T_1 precipitate with one unit cell in thickness; (c), a GPT_1 zone nucleating on a well-development T_1-precipitate; (d), the T_1-precipitate with two unit cells in thickness [43]

Figure 2-15 reveals the TYPE-II coarsening phenomenon. In Figure 2-15b, a space of d_{111Al} can be observed between the upper and lower unit cells, and the upper one moves

doi:10.6342/NTU202402902

by 1/6<112>$_{Al}$ in relation to the lower one. Further observations from the [110] zone axis in Figure 2-15c and d show that, compared to TYPE-I coarsening, there is an additional layer of atoms between the unit cells. Both types of coarsening mechanisms frequently occur during peak aging, with TYPE-I being more commonly observed.

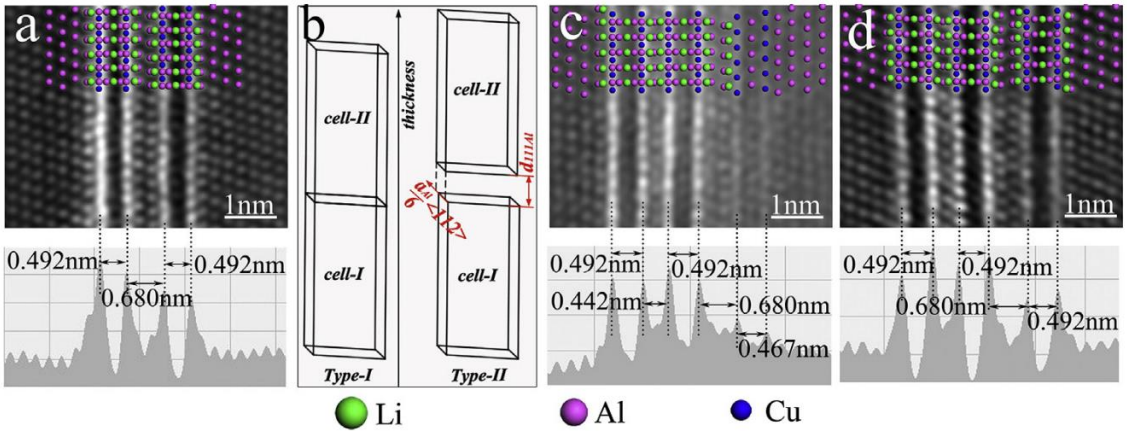

Figure 2-15 (a) An abnormal T_1 with two misaligned T_1 unit cells. (b) A schematic illustration for the normal and abnormal growth mechanism of the T_1. (c, d) Another variant of the abnormal T_1 thickening in the second growth mechanism: a normal 2-unit-cell-thick T_1 plus a misaligned 1-unit-cellthick T_1 [43]

2.1.6 Precipitation Hardening

The primary principle behind precipitation hardening is that precipitates impede dislocation slip and pin dislocations, thereby enhancing the material's strength [45, 46]. The effectiveness and mechanism of strengthening are primarily influenced by five factors: precipitate size, volume fraction, location, particle-matrix interface, and crystal structure.

doi:10.6342/NTU202402902

Generally, for precipitates that are coherent with their matrix, the force acting on a mobile dislocation in a stressed metal containing particles is illustrated in Figure 2-16. By examining the balance of forces between the dislocation's line tension T and the resistance force F exerted by the particles, it can be understood that in Equation 2-1:

$$F = 2T\sin\theta$$

As F increases, the phenomenon of dislocation bowing also increases, and θ rises correspondingly. When the line tension force reaches its maximum value, where $\sin\theta = 1$, F exceeds $2T$, resulting in the dislocation bypassing the particle via Orowan looping [47], while leaving the precipitate unchanged. This transformation process is illustrated in Figure 2-17.

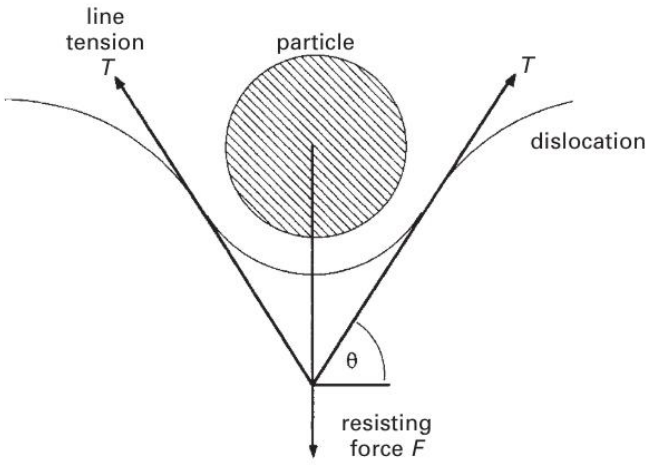

Figure 2-16 Balance of forces acting during particle resistance to dislocation movement

doi:10.6342/NTU202402902

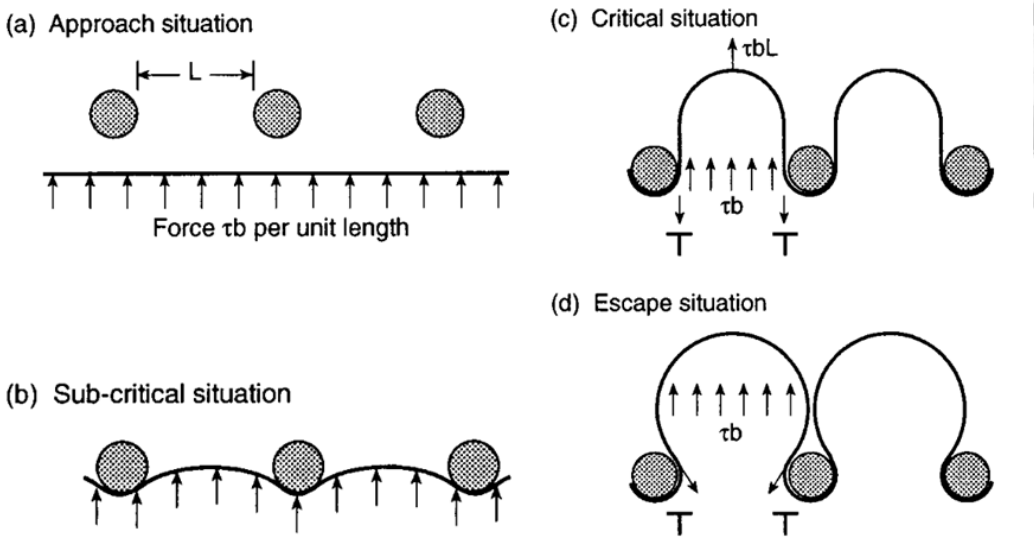

Figure 2-17 The schematic of Orowan looping mechanism [45]

However, if $F < 2Tsin\theta$, meaning the resistance force of the precipitate is less than the dislocation line tension, the particle will be sheared, and the dislocation will pass through the particle, leaving behind a Burgers vector, as shown in Figure 2-18.

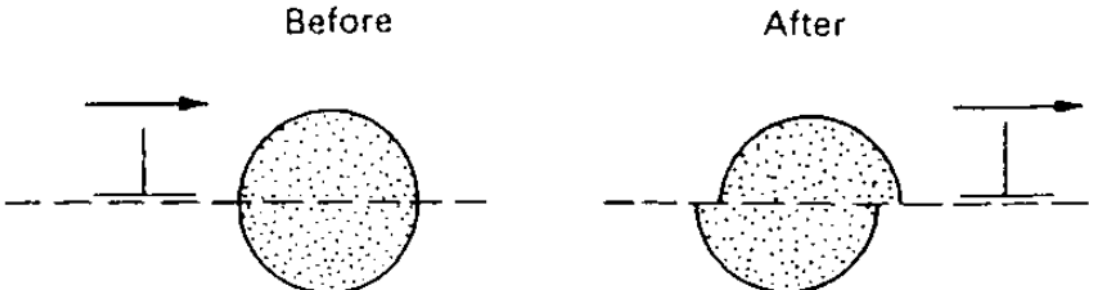

Figure 2-18 The schematic of particle cutting mechanism [45]

According to past mechanical models, the size of the particle affects the strengthening mechanism and the strength achieved. As shown in Figure 2-19, with the same volume fraction, smaller particle sizes require a relatively lower shear stress to

doi:10.6342/NTU202402902

activate the cutting mechanism. In this case, cutting dominates the strengthening mechanism until the particle reaches a critical size, where the highest strengthening effect is observed. However, beyond the critical size, the shear stress needed to drive Orowan looping is lower than that for cutting, causing a shift in the strengthening mechanism. Finally, the higher the particle strength, the higher the strength required for cutting, shifting the gray line in Figure 2-19 upwards, and consequently reducing the critical particle size.

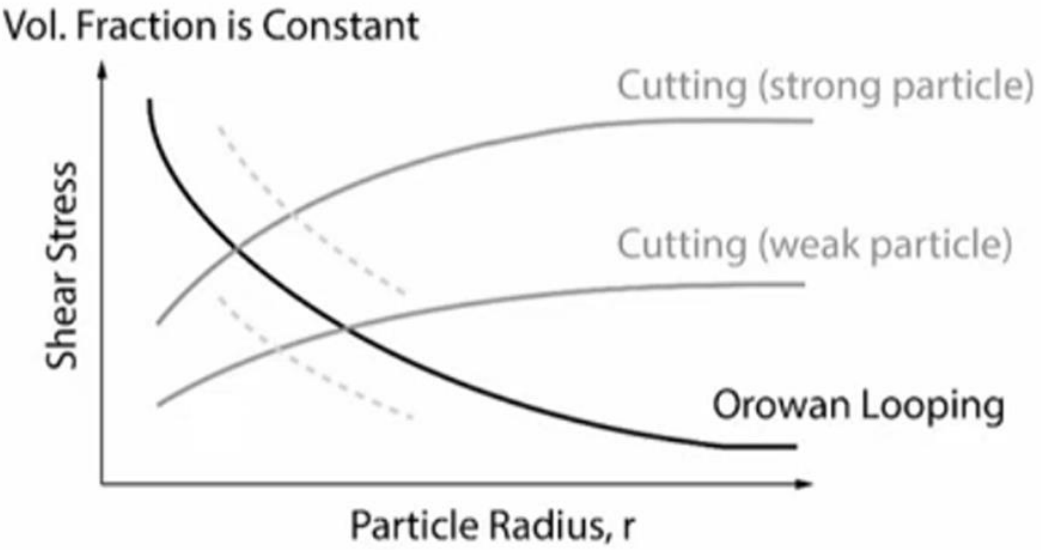

Figure 2-19 Relationship between Shear Stress and Particle Radius, with Particle Volume Fraction Fixed

doi:10.6342/NTU202402902

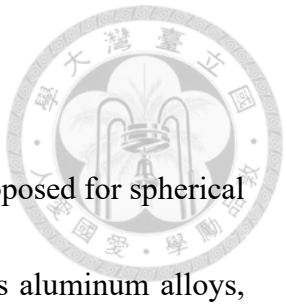

2.1.7 Shearing Behavior of T_1 Precipitates

The critical size model discussed in the previous section was proposed for spherical precipitates. Although spherical precipitates also exist in 2000 series aluminum alloys, the primary strengthening phase, T_1, is plate-like with a large aspect ratio, making this model inapplicable [48]. Therefore, a detailed discussion of the precipitation hardening mechanism of T_1 is necessary.

Historically, T_1 precipitates were generally considered a strong, unshearable phase. However, recent experiments have overturned this theory. TEM observations have revealed the cutting morphology of one-layer T_1 [49], as shown in Figure 2-20b. It was found that dislocations slip on the {111} planes other than the growth plane, cutting through T_1 and creating a Burgers vector, as depicted in Figure 2-20a and c.

In 2014, Dorin et al. conducted additional aging at 190°C on peak-aged specimens to study the coarsening and strengthening mechanism of T_1 [50]. They observed the interaction between dislocations and T_1 precipitates of different layers. It was discovered that T_1 precipitates with up to three layers could be cut by dislocations, while no cutting mechanism was observed for four-layer T_1 structures, as shown in Figure 2-21. Additionally, they observed that after high-temperature aging and coarsening of T_1, the strain hardening rate continued to increase. This indicates that the strengthening mechanism gradually transitions from cutting to Orowan looping. Unlike spherical

doi:10.6342/NTU202402902

precipitates, plate-like T_1 precipitates do not have a clear critical thickness for this transition. Both mechanisms may occur simultaneously within the same precipitate, making the process more complex than for spherical precipitates. Further research is expected to provide deeper insights into this phenomenon.

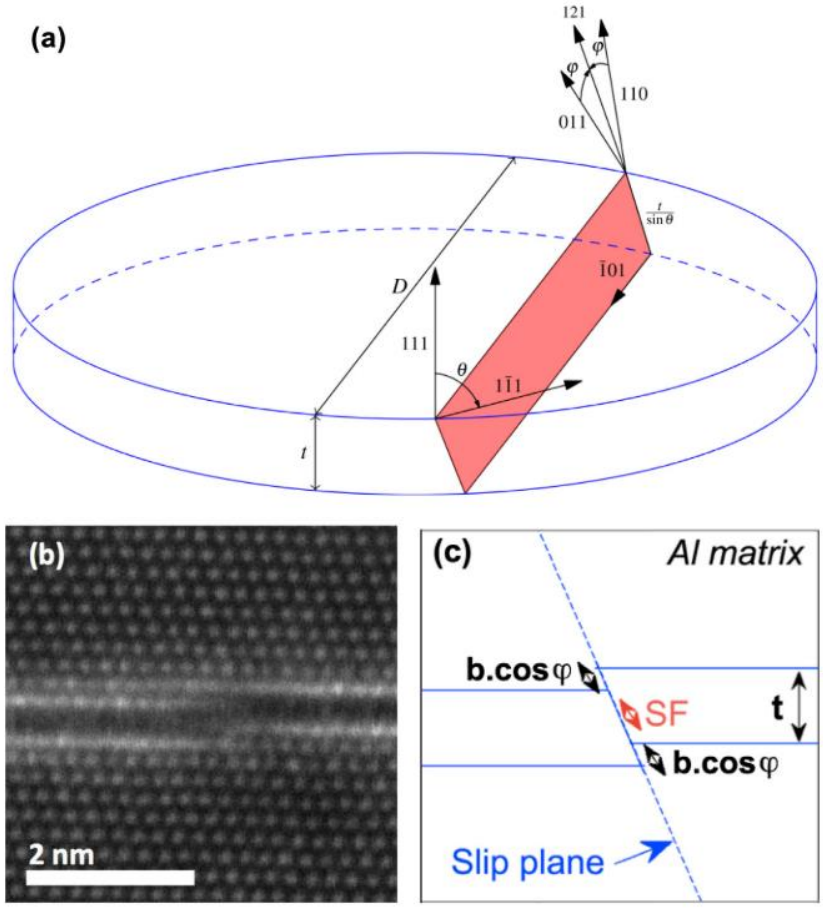

Figure 2-20 (a) Scheme of a disc-shaped T_1 plate and the trace of the matrix glide plane within the precipitate. The <110> directions possible for the matrix Burgers vector are indicated, as well as the angles used in the model. (b) Image of a sheared T_1 taken in HAADF-STEM along a [110] zone axis. (c) Relationship between the observed step size on this image and the geometrical parameters of (a). [49]

doi:10.6342/NTU202402902

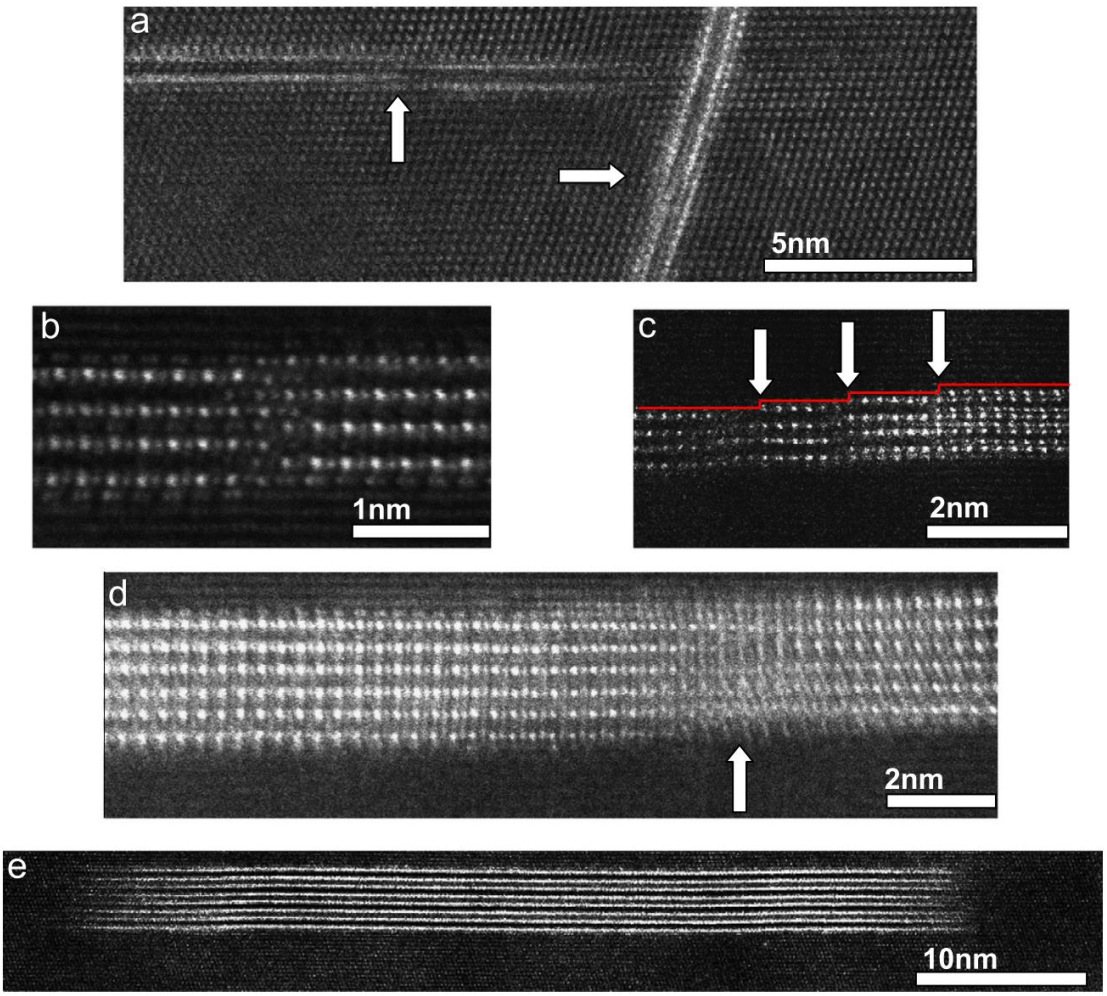

Figure 2-21 HAADF-STEM images taken on a sample aged 18 h at 155°C and 70 h at 190°C and then deformed plastically 2%. (a)–(d) single to three-layer T_1 precipitates that have all been sheared and (e) a four-layer T_1 that has not been sheared. [50]

doi:10.6342/NTU202402902

2.2 Different Aging Treatments

In this section, we will discuss methods to increase T_1 precipitation. Section 2.2.1 covers the effect of introducing dislocations into the material before aging, a process we refer to as pre-strain. Section 2.2.2 discusses an advanced processing method called creep age forming (CAF), which involves applying stress during aging to shape the material at high temperatures.

2.2.1 Pre-Strain Aging Treatment

In current aerospace aluminum alloy manufacturing, a stretching process is typically performed after solution treatment to release residual stresses from quenching. This stretching usually ranges between 2-5% [51]. For third-generation aluminum alloys, this post-quenching strain introduces dislocations into the material, known as pre-strain. Pre-strain significantly aids in the heterogeneous nucleation of T_1, resulting in increased T_1 precipitation within the matrix and improved mechanical properties[51-54]. As shown in Figure 2-22, the yield strength of materials with 0% pre-strain is noticeably lower than those with pre-strain.

doi:10.6342/NTU202402902

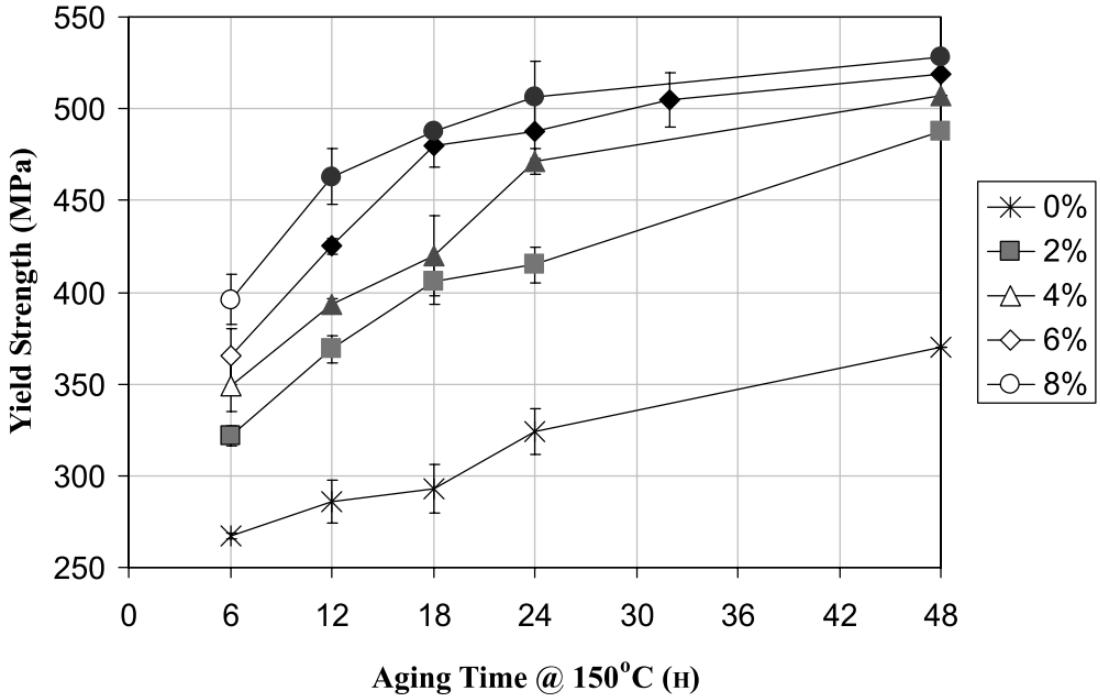

Figure 2-22 Yield strength after aging under different pre-strain conditions [53]

Increased T_1 precipitation in the matrix also helps to prevent precipitation at grain boundaries, which can negatively affect toughness [51]. Additionally, the increased T_1 precipitation consumes more Li elements, reducing the formation of the weaker δ' phase. Figure 2-23 shows that the T_1 density in pre-strained specimens is significantly higher than in non-pre-strained specimens within the same field of view. This is also evident in the diffraction pattern, where the diffraction contribution from the δ' phase is reduced, as indicated by the blue circles in Figure 2-23.

doi:10.6342/NTU202402902

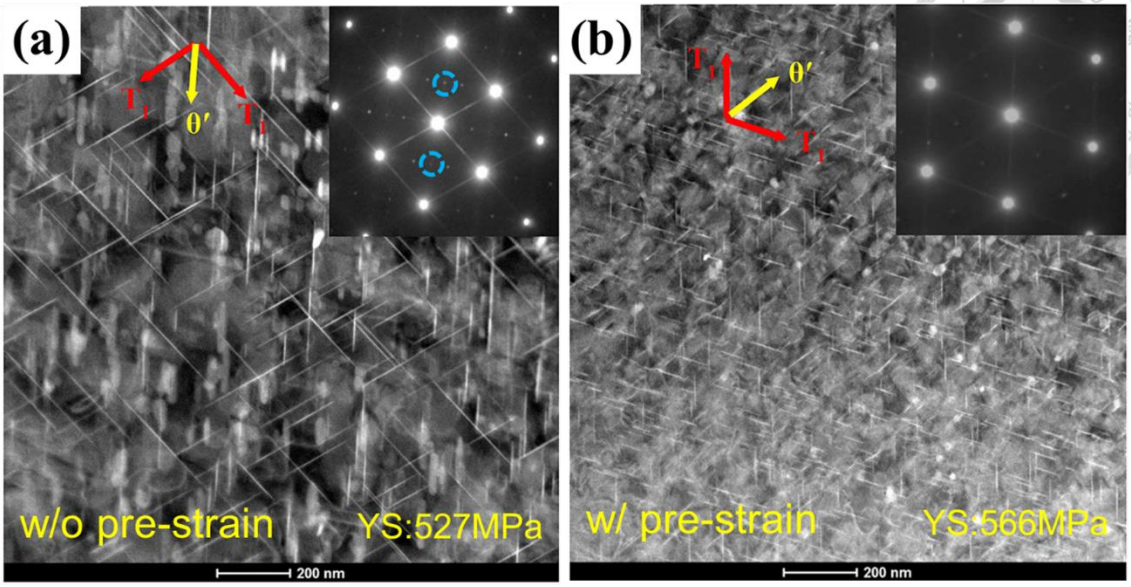

Figure 2-23 HAADF-STEM images taken along the $[110]_{Al}$ direction and the corresponding SAED patterns of (a) without pre-strain and (b) with pre-strain [54]

2.2.2 Creep Age Forming (CAF)

Creep age forming is a specialized process for aluminum alloys that involves applying external stress during artificial aging. This process enhances mechanical properties while plastically forming components, making it ideal for producing large aerospace panels [55]. As illustrated in Figure 2-24, the process begins by placing the solution-treated panel on a forming tool and creating a vacuum, forcing the workpiece to conform to the tool shape due to atmospheric pressure. For stronger workpieces, mechanical clamping can supplement the vacuum. Next, the assembly is heated to the aging temperature and held for a specified period. Finally, after cooling to room temperature and releasing the pressure, the workpiece springs back to a shape between its undeformed state and the tool shape.

doi:10.6342/NTU202402902

Currently, many studies incorporate a pre-strain step before CAF to further enhance T_1 precipitation efficiency [54, 56]. However, the details of this strengthening mechanism are not yet fully understood and require further clarification.

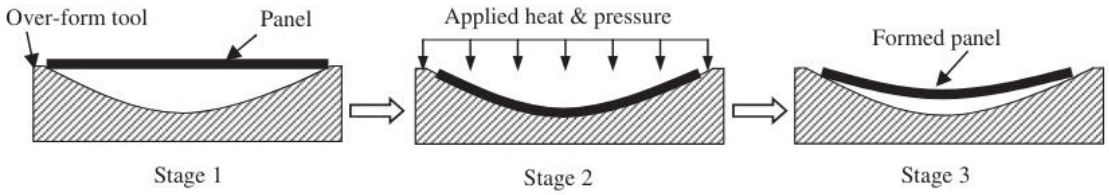

Figure 2-24 The schematic diagram of creep age forming [55]

2.3 Advanced Analytical Technique

In this section, we will discuss two advanced material analysis techniques: integrated differential phase contrast (iDPC), which is capable of simultaneously imaging both light and heavy elements, and small-angle X-ray scattering (SAXS), which provides comprehensive information on the size distribution of nanoscale precipitates.

2.3.1 Integrated Differential Phase Contrast (iDPC)

In the past 20 years, TEM resolution has significantly improved from 200 pm to 50 pm, thanks to advancements in Cs-corrector technology. This increase in resolution has led to higher measurement accuracy and opened new possibilities for atomic-scale analysis. Typically, atomic-level imaging uses HAADF-STEM, where image contrast is roughly proportional to the square of the atomic number (Z), hence the name Z contrast

doi:10.6342/NTU202402902

imaging [57]. However, this technique is insensitive to light elements like oxygen, nitrogen, carbon, boron, and lithium when imaging alongside heavier atoms such as silicon, gallium, strontium, and gold. Therefore, modern aberration-corrected STEM instruments usually only resolve elements with relatively high scattering power.

Recently, a novel STEM technique called iDPC-STEM imaging has been introduced. This method offers truly linear imaging for thin specimens. For non-magnetic samples, the sample's electric field (a conservative vector field) is the gradient of its electrostatic potential field (a scalar field). Thin samples cause electron deflection proportional to their in-plane components. This deflection is measured by detecting electron positions on a far-field detector, providing information about the center of mass (COM) position [58].

Figure 2-26 illustrates the iDPC-STEM schematic. By measuring A-C and B-D, COMx and COMy can be obtained, and high-quality images can be calculated through illustrates the iDPC-STEM schematic. By measuring A-C and B-D, COMx and COMy can be obtained, and high-quality images can be calculated through fitting. The imaging process relies on the atomic number, with higher atomic numbers resulting in stronger scattering and brighter signals. The intensity in iDPC images is linearly related to the atomic number. Figure 2-25 shows the brightness of different elements in iDPC and ADF images, demonstrating that iDPC can reveal elements with lower atomic numbers.

Compared to HAADF-STEM, iDPC-STEM significantly improves the detectability

doi:10.6342/NTU202402902

of light elements among heavy elements in a single image. For example, we can accurately identify the position of Li in T_1 (Al_2CuLi) precipitates. Knowing the position of Li is crucial for studying precipitate evolution or cutting mechanisms. Currently, there are no documented cases of Li in T_1 being imaged. Chapter 5.4 of this thesis will present iDPC images of T_1, showcasing the position of Li atoms.

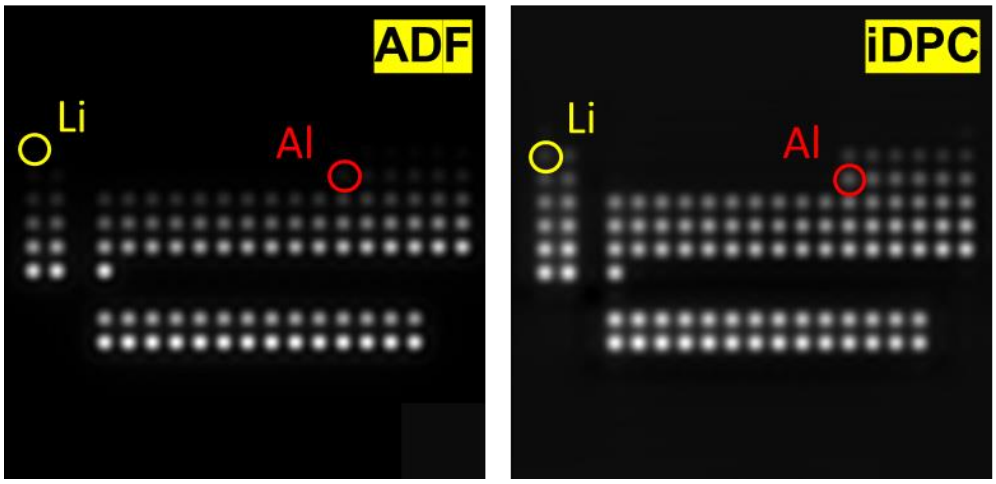

Figure 2-25 The comparison of single-atom contrast in the range Z = 1–103 obtained by simulations: (a) ADF-STEM image (b) iDPC-STEM image [58]

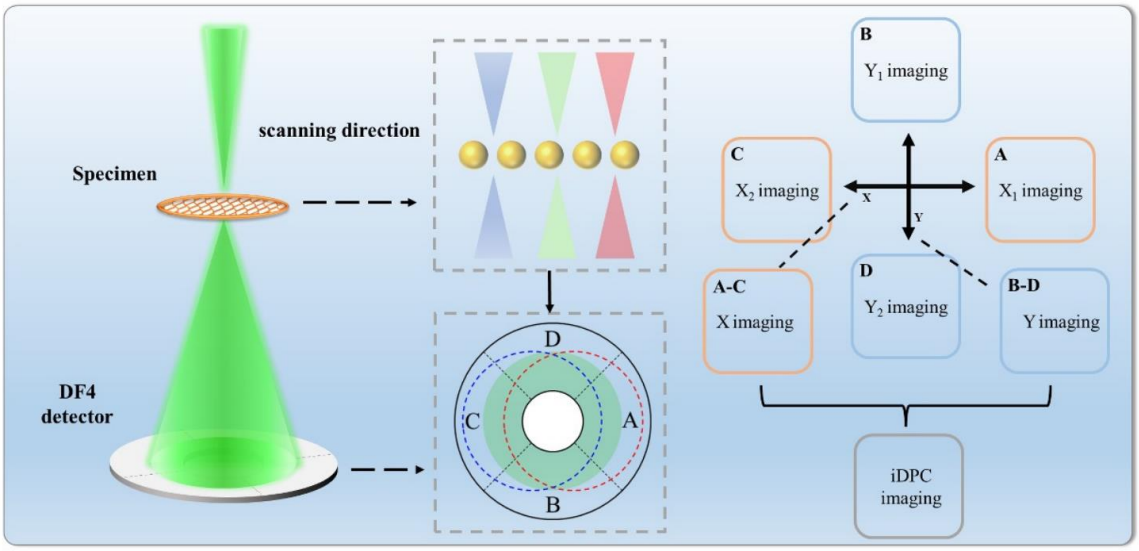

Figure 2-26 The schematic diagram of technical principle: partition probe, electrostatic potential imaging, and integral [58]

doi:10.6342/NTU202402902

2.3.2 Small-Angle X-ray Scattering (SAXS)

Because the observation range of materials using TEM is limited, it is difficult to obtain comprehensive statistical data on the size and dimensions of precipitates. In this case, Small-Angle X-ray Scattering (SAXS) is an excellent method. Its observation range is approximately 500μm x 500μm, and the thickness of the AA2050 sample is about 30μm. Therefore, the statistically significant sample size makes the results more representative.

The basic theory of SAXS can be illustrated by Figure 2-27. When the incident X-ray ($\mathbf{s_0}$) advances and encounters a scattering point P, the distance between the two points is denoted by **r**, which results in scattering. We consider the scattered light at an angle θ to the direction of the incident light (θ is called the scattering angle), with **s1** being the unit vector in the direction of this scattered light. The amplitude of the scattered wave is A1. Similarly, the scattering point O also produces a scattered wave with amplitude A2. The intensity of the scattered light we detect is determined by the addition of these two wave amplitudes. When performing this addition, we must consider the phase difference ($\Delta\emptyset$) between the two waves, which is related to the path length difference (δ) that the two waves travel before reaching the detector. This can be expressed as:

$$\Delta\emptyset = \frac{2\pi\delta}{\lambda}$$

doi:10.6342/NTU202402902

Where λ is the wavelength of the X-ray. Since $\delta = \overline{QP} - \overline{OR}$, and $\overline{QP} = \boldsymbol{r} \cdot \boldsymbol{s_0}$, $\overline{OR} = \boldsymbol{r} \cdot \boldsymbol{s_1}$, We have:

$$\Delta\emptyset = \frac{2\pi\delta}{\lambda} = -\frac{2\pi(\boldsymbol{s_1} - \boldsymbol{s_0}) \cdot \boldsymbol{r}}{\lambda} = -\boldsymbol{q} \cdot \boldsymbol{r}$$

Where $\boldsymbol{q} = 2\pi(\boldsymbol{s_1} - \boldsymbol{s_0})/\lambda$ is called the scattering vector, and its magnitude is $q = 4\pi \sin\left(\frac{\theta}{2}\right)/\lambda$.

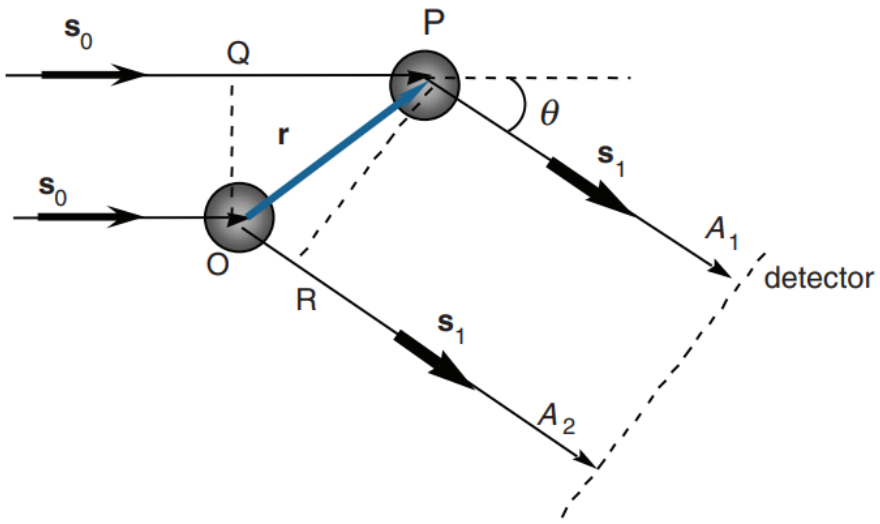

Figure 2-27 Schematic diagram of light scattering by particles

The raw signal detected by CCD, as shown in Figure 2-28, is a 2D pattern. The center serves as the starting point of the scattering vector q. By performing azimuthal integration, we can obtain a one-dimensional plot of scattering intensity I(q) versus q. This plot can be used for subsequent fitting calculations to derive information on the precipitate size and volume fraction. Additionally, some information can be known directly from the 2D

doi:10.6342/NTU202402902

pattern. For example, streak-like features in the pattern may indicate precipitates with a large aspect ratio, such as GP zones. As heating time increases, the disappearance of streaks in the 2D pattern suggests the dissolution of GP zones [59].

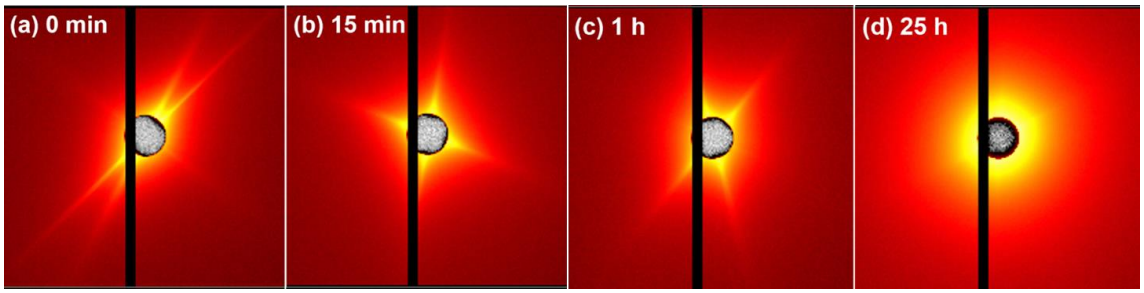

Figure 2-28 Evolution of SAXS 2D pattern of cold-rolled $Al_{0.2}CoCrFeNi$ Alloy Aged at 550°C for (a) 0 min, (b) 15 min, (c) 1 h, and (d) 25 h [59]

doi:10.6342/NTU202402902

Chapter 3 Experimental Procedures

3.1 Experimental Process

This study utilizes AA2050-T8 third-generation aluminum-lithium alloy plates produced by Constellium, with a thickness of 3mm. The chemical composition of the alloy, as detailed in Table 3-1, was reconfirmed through the use of an Inductively Coupled Plasma Mass Spectrometry (ICP-MS) instrument to ensure accuracy.

Table 3-1 Chemical composition of AA2050-T8

Alloy	**Al**	**Cu**	**Li**	**Mg**	**Ag**	**Mn**	**Zn**	**Zr**
wt%	Bal.	3.68	0.96	0.34	0.35	0.38	0.25	0.09

3.1.1 Pre-Strain Aging Treatment (PA) and Pre-Strain Creep Aging Treatment (PCA)

The alloys in this study were subjected to two different heat treatments as illustrated in Figure 3.1. Initially, all samples underwent a solution heat treatment at 500°C for 1 hours, followed by water quenching within a transfer time of 1.5 seconds. They were then pre-strained by 5% at room temperature. Subsequently, the PA samples were subjected to isothermal aging at 155°C for 20 hours. In contrast, the PCA samples underwent aging at 155°C for 20 hours while a constant tensile stress of 175 MPa was simultaneously applied.

doi:10.6342/NTU202402902

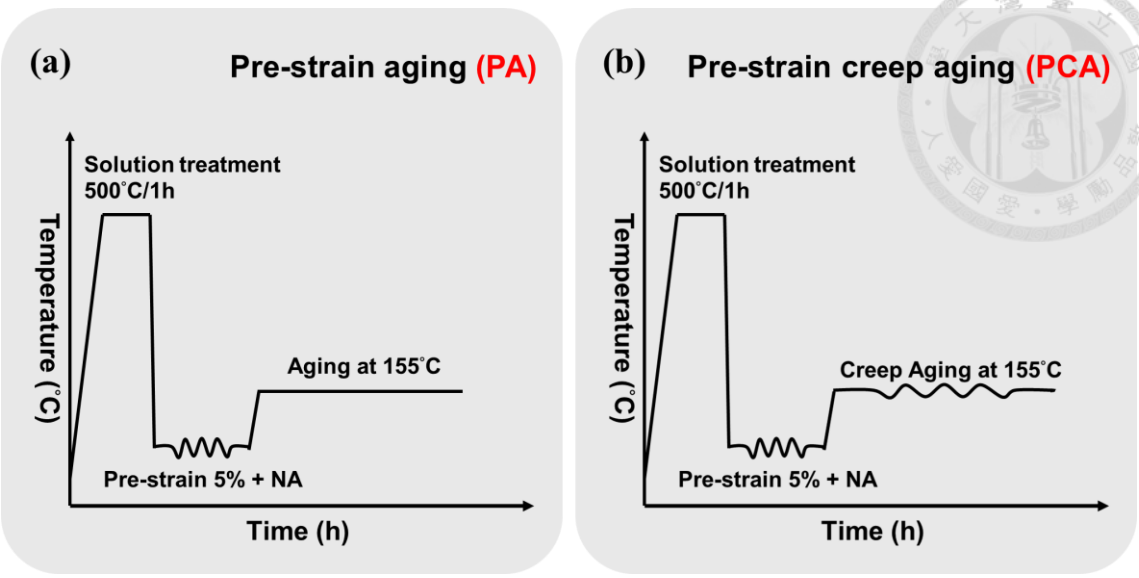

Figure 3-1 (a) Pre-strain aging treatment (b) Pre-strain creep aging treatment

3.2 Sample Preparation

3.2.1 Universal Testing Machine

Both the pre-strain and creep aging processes were conducted using the YM-H5103-A01 Universal Testing Machine from Yang Yi Technology, equipped with a CDV-500HS hot air circulation oven. The universal testing machine boasts a maximum tensile force capacity of 100 kN, with a force resolution of 0.5 N and a travel resolution of 0.001 mm. The hot air circulation oven can reach a maximum temperature of 500˚C, with a temperature precision of ±1˚C and a distribution of ±2˚C.。

doi:10.6342/NTU202402902

3.2.2 Twin-Jet Polisher

TEM sample was performed using a twin-jet polisher manufactured by E.A. Fischione Instruments. Initially, samples from PA and PCA treatments were prepared by cutting discs and mechanically thinning them to 0.07 mm. Subsequent electropolishing was conducted using the twin-jet polisher in a solution of 30% nitric acid and 70% methanol at -25°C with a working voltage of 12V. Finally, the samples were cleaned with anhydrous alcohol and isopropyl alcohol and then preserved under vacuum.

3.3 Mechanical Test

3.3.1 Tensile Test

Mechanical properties such as Yield Strength (YS), Ultimate Tensile Strength (UTS), and Elongation (EL) were determined through tensile tests conducted using the MTS Landmark servo-hydraulic dynamic testing system, which has a maximum stress capacity of 25 kN. This system is equipped with a laser extensometer for accurate strain measurement. The tensile tests were performed at room temperature with a strain rate of 0.001 s^-1. Samples were machined into tensile specimens as shown in Figure 3-2.

doi:10.6342/NTU202402902

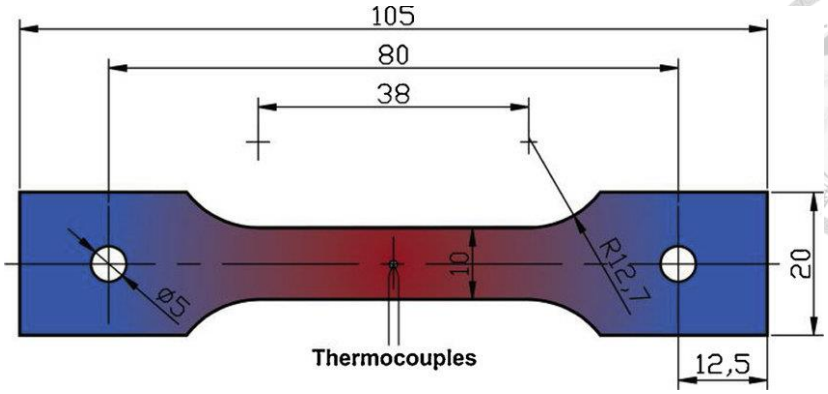

Figure 3-2 Specimen of hot tensile testing

3.3.2 Vickers Hardness Test

The hardness testing employed in this study utilizes the Vickers hardness test. This method involves pressing a diamond indenter with a square base into the material's surface. The diagonal lengths of the indentation are measured to calculate the Vickers hardness (HV), as shown in Figure 3-3. For this specific test, a load of 500 grams and a duration of 8 seconds were applied. Each hardness value reported is derived from an average of 20 measurements. For the hardness test sample preparation, specimens were mechanically ground using SiC sandpaper up to 2500 grit.

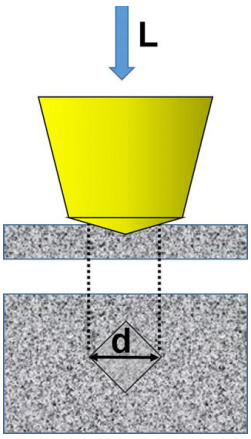

Figure 3-3 Vickers micro-indentation test [60]

doi:10.6342/NTU202402902

3.4 Microstructure Characterization

3.4.1 Transmission Electron Microscopy (TEM)

The principle of TEM involves high-voltage electron beams penetrating the specimen and collecting signals from scattered and transmitted electrons for analysis. In this study, we utilized the FEI Tecnai G2 F20 and Thermo Fisher Scientific Talos F200X G2 TEMs, both operating at an accelerating voltage of 200 kV. The bright-field images in this study were acquired using direct beam imaging. High-Resolution Scanning Transmission Electron Microscopy (HR-STEM) and integrated differential phase contrast STEM (iDPC-STEM) images were captured using a Thermo Fisher Spectra 300 TEM, equipped with dual spherical aberration correctors, achieving a maximum resolution of 50 pm at 300 kV.

3.4.2 Small-Angle X-ray Scattering (SAXS)

The SAXS experiments were conducted at the BL23A SWAXS beamline of the Taiwan Light Source (TLS) at the National Synchrotron Radiation Research Center (NSRRC). The SAXS beam energy was 15 keV, corresponding to an incident wavelength of 0.83 Å. The optimal sample thickness for AA2050 was calculated to be 38.7 μm, with a sample collection volume of approximately 500 μm × 500 μm × 38.7 μm, and a collection time of 100 seconds.

doi:10.6342/NTU202402902

The experimental setup involved collecting 2D X-ray scattering patterns using a CCD detector, as shown in Figure 3-4. These patterns were then processed using data reduction software to generate I(q) versus q data, where q is the scattering vector. The final analysis was performed using SASVIEW software, fitting the data with mathematical models to obtain the results.

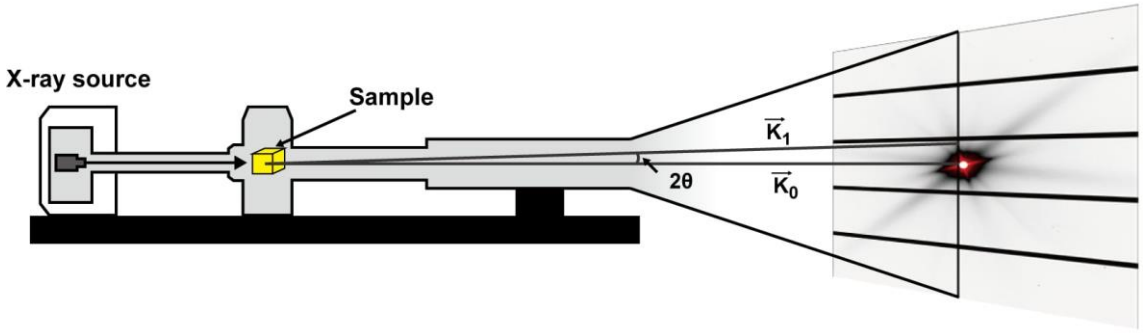

Figure 3-4 Schematic diagram of SAXS operation

doi:10.6342/NTU202402902

Chapter 4 Results of Different Aging Treatments on Pre-strain Al-Cu-Li Alloy

In this chapter, we first discuss whether the solution heat treatment (SHT) achieved the goal of solute dissolution. Then, sections 4.2 and 4.3 analyze the TEM images at various stages of pre-strain aging and pre-strain creep aging. Section 4.4 focuses on measuring the size of T_1 precipitates in the matrix, and section 4.5 presents the mechanical property measurements.

4.1 Solution Heat Treatment (SHT)

In this section, we examine the impact of solution heat treatment (SHT) on the as-received AA2050-T8 alloy. The primary objective of the SHT process is to achieve uniform dissolution of solute elements such as Cu, Li, Mg, and Ag into the matrix, thereby optimizing subsequent precipitation behavior.

Initial hardness measurements were taken on the as-received material, as illustrated in Figure 4-1a. The as-received exhibited a hardness value of 162 HV. Following SHT at 500°C for 1 hour, the hardness significantly decreased to 82 HV, indicating a reduction of 80 HV. This reduction suggests that the precipitates had dissolved back into the matrix, thereby diminishing the precipitation hardening effect.

Similarly, a tensile test was conducted, as shown in Figure 4-1b. The as-received

doi:10.6342/NTU202402902

sample exhibited higher mechanical strength, whereas the as-quenched sample showed lower strength and higher ductility. Additionally, a serrated stress-strain curve was observed, known as the Portevin–Le Chatelier (PLC) effect, or dynamic strain aging (DSA). This effect arises from the interaction between moving dislocations and diffusing solute atoms. When dislocations move, they encounter solute atoms that temporarily pin them, leading to an increase in local stress. As the stress builds up, the dislocations break free, causing a sudden drop in stress and serrations in the stress-strain curve. This phenomenon indicates that solute atoms are dispersed in the matrix in the as-quenched state, further confirming the effectiveness of the SHT.

The summarized data from hardness and tensile tests are presented in Table 4-1. The results from these tests indicate that SHT at 500°C for 1 hour is effective in dissolving solute atoms back into the matrix, thereby validating the process's effectiveness.

doi:10.6342/NTU202402902

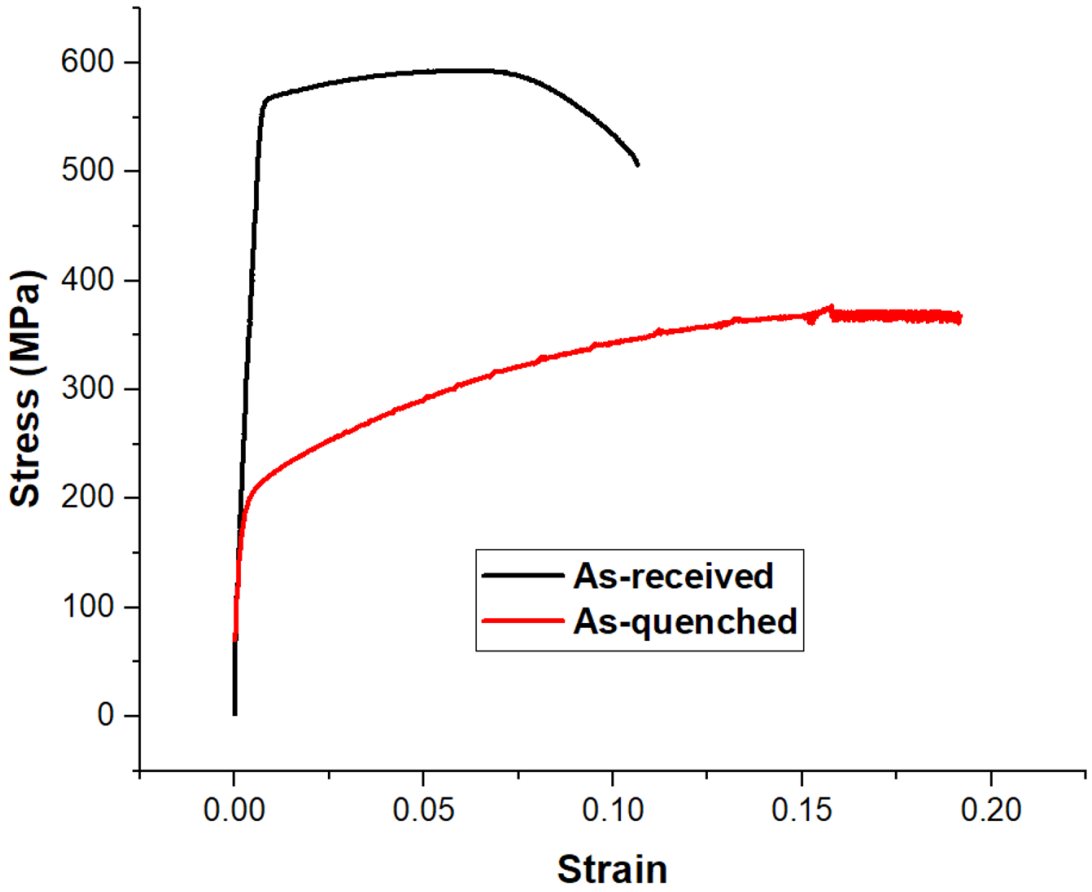

Figure 4-1 Tensile results of as-received and as-quenched specimen

Table 4-1 Mechanical properties of as-received and as-quenched specimen

	YS (MPa)	UTS (MPa)	EL (%)	Hardness (HV)
As-received	569.1	592.7	10.7	162.45±3.7
As-quenched	207.2	376.9	19.2	82.74±2.3

4.2 Pre-Strain Aging

In this section, we discuss the effect of pre-strain aging on AA2050. After undergoing SHT, the material was subjected to a 5% strain followed by aging at 155°C to induce precipitation hardening.

doi:10.6342/NTU202402902

To determine the peak aging time, hardness measurements were taken every two hours over 30 hours, as shown in Figure 4-2. The material reached its peak hardness of 162.3 HV at 20 hours. Samples were taken at 4, 8, 14, and 20 hours to observe precipitate evolution, which will be detailed in subsequent chapters. Notably, there was a decrease in hardness during the first 0-2 hours. This phenomenon, observed in many 2xxx series aluminum alloys, is attributed to the dissolution of clusters during early aging stages, as suggested by previous Small-Angle X-ray Scattering (SAXS) studies.

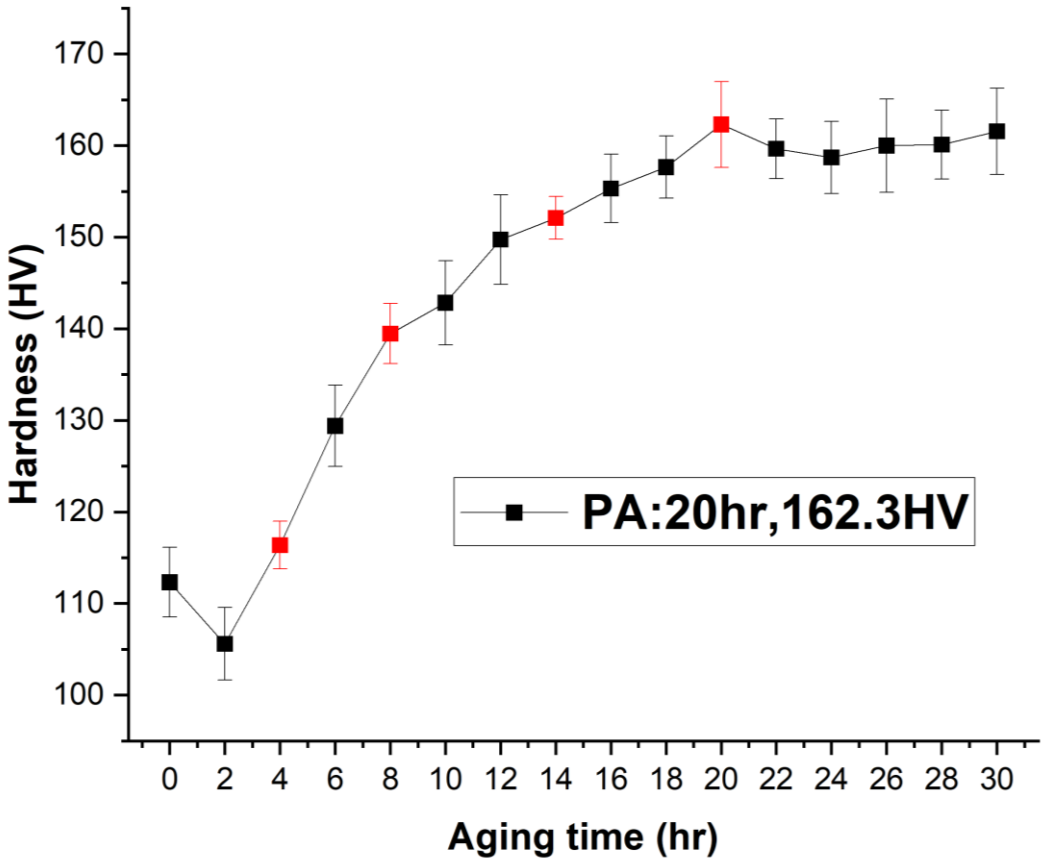

Figure 4-2 Hardness result of pre-strain aging

doi:10.6342/NTU202402902

4.2.1 Pre-Strain Aging 4 Hours (PA4)

After 4 hours of artificial aging following pre-strain, numerous dislocations can be observed in the bright-field TEM images along the [110] zone axis, as shown in Figure 4-3a. Many T_1 precipitates have grown on these dislocations, indicating a tendency for T_1 precipitates to nucleate heterogeneously. This phenomenon is further evidenced in the high-magnification image in Figure 4-3b. Additionally, atomic-scale imaging at the white arrows shows that the T_1 precipitates are primarily single-layered at this stage, while the blue circles indicate the presence of a small amount of θ' precipitates.

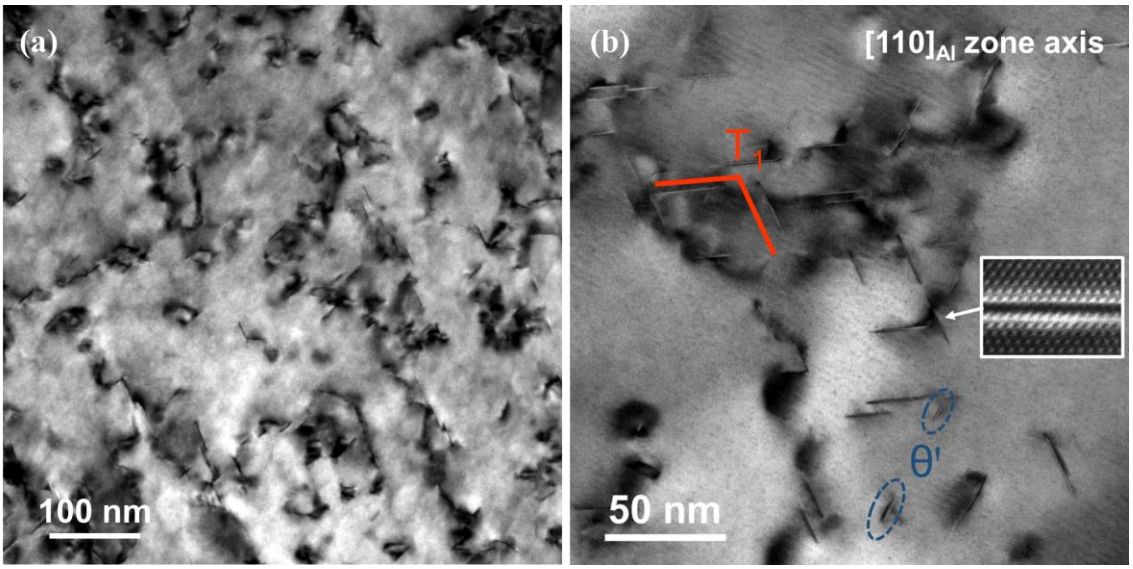

Figure 4-3 TEM BF images of PA4 process along the $[110]_{Al}$ zone axis

doi:10.6342/NTU202402902

4.2.2 Pre-Strain Aging 8 Hours and 14 Hours (PA8 and PA14)

After 8 hours of artificial aging following pre-strain, it is evident from Figure 4-4a that the diameters of T_1 and θ' precipitates have significantly increased compared to PA4. Continuing the aging process to 14 hours, as shown in Figure 4-4b, reveals a slight increase in precipitate size compared to the PA8, although not very prominently.

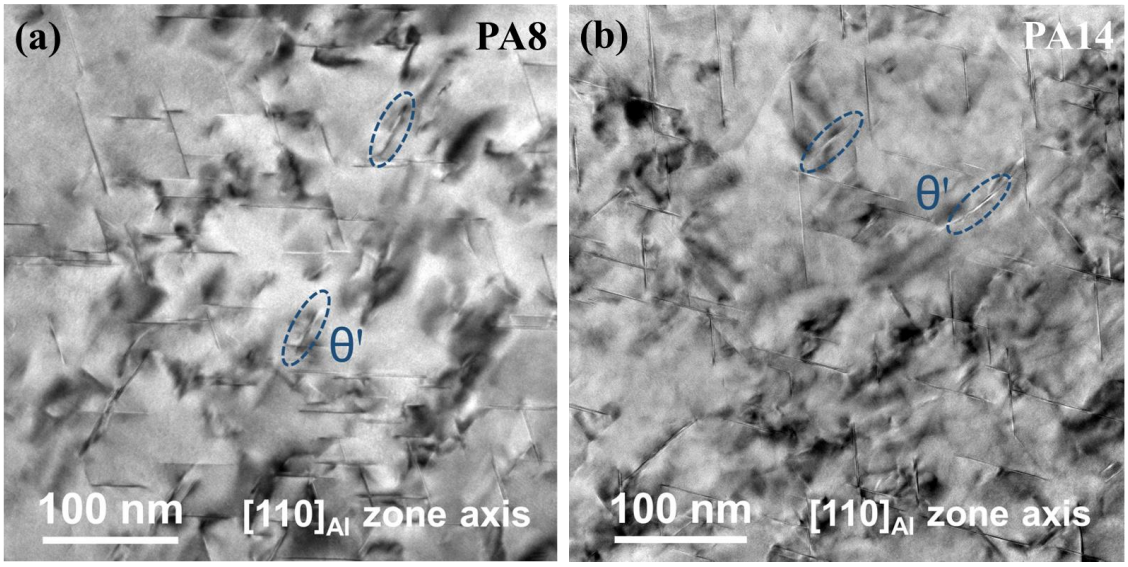

Figure 4-4 TEM BF images of (a) PA8 (b) PA14 process along the $[110]_{Al}$ zone axis

When the zone axis is changed to [112] for observation, as shown in Figure 4-5a, only one type of edge-on T_1 precipitate can be observed in the same direction. Magnifying the area indicated by the white arrows to the atomic scale reveals that, compared to the PA4, the T_1 precipitates have not thickened and remain as one layer. Additionally, a small amount of edge-on S precipitates can be observed in the area indicated by the yellow circles. The presence of S precipitates is further confirmed by the FFT diffraction pattern shown in Figure 4-5b.

doi:10.6342/NTU202402902

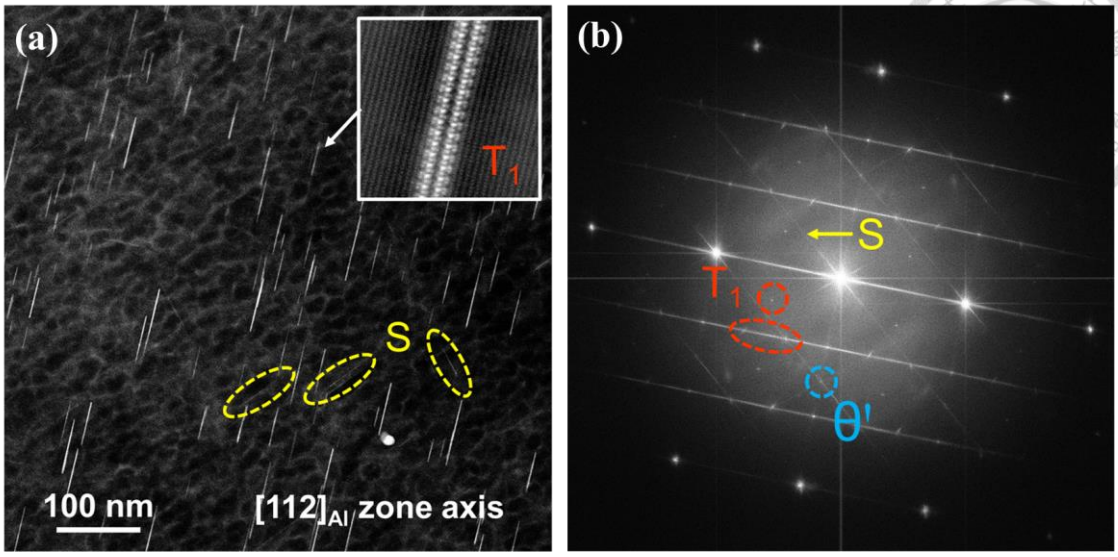

Figure 4-5 (a) HAADF-STEM image of PA14 process along the $[112]_{Al}$ zone axis (b) The FFT diffractogram

4.2.3 Pre-Strain Aging 20 Hours (PA20)

At the peak aging time, which is pre-strain aging for 20 hours, the T_1 precipitates have grown to the optimal size and density to provide the material with maximum strength, as shown in Figure 4-6. The quantitative results regarding the size of these precipitates will be discussed in subsequent chapters.

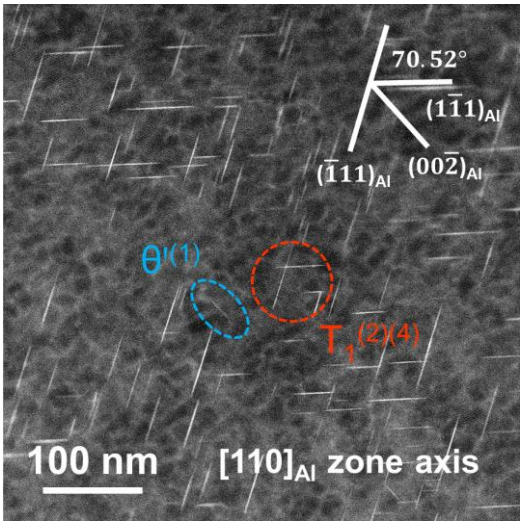

Figure 4-6 HAADF-STEM image of PA20 process along the $[110]_{Al}$ zone axis

doi:10.6342/NTU202402902

During peak aging, directional shadow images are observed in both bright-field and dark-field images, as indicated by the red circles in Figures 4-7c and 4-7d. These shadows are attributed to the strain fields formed by the intergrowth of the precipitates. Figure 4-4b illustrates the orientation relationships of T_1. Generally, in the [110] zone axis, $T_1^{(2)}$ and $T_1^{(4)}$ are observed as edge-on, while $T_1^{(1)}$ and $T_1^{(3)}$ are non-edge-on and thus cannot be observed because the contrast is too low. However, at peak aging, the $T_1^{(1)}$ and $T_1^{(3)}$ precipitates grow larger and frequently intergrow. The strain fields from the intergrowth of $T_1^{(1)}$ and $T_1^{(3)}$ create shadow images in the bright-field and dark-field images, which are parallel to $\theta'^{(1)}$.

Further confirmation is provided by Figure 4-7a, where no shadow images are observed in the HAADF image, but brighter contrast is seen in the same locations. This brighter contrast is due to the heavier elemental composition within the intergrown T_1 precipitates.

doi:10.6342/NTU202402902

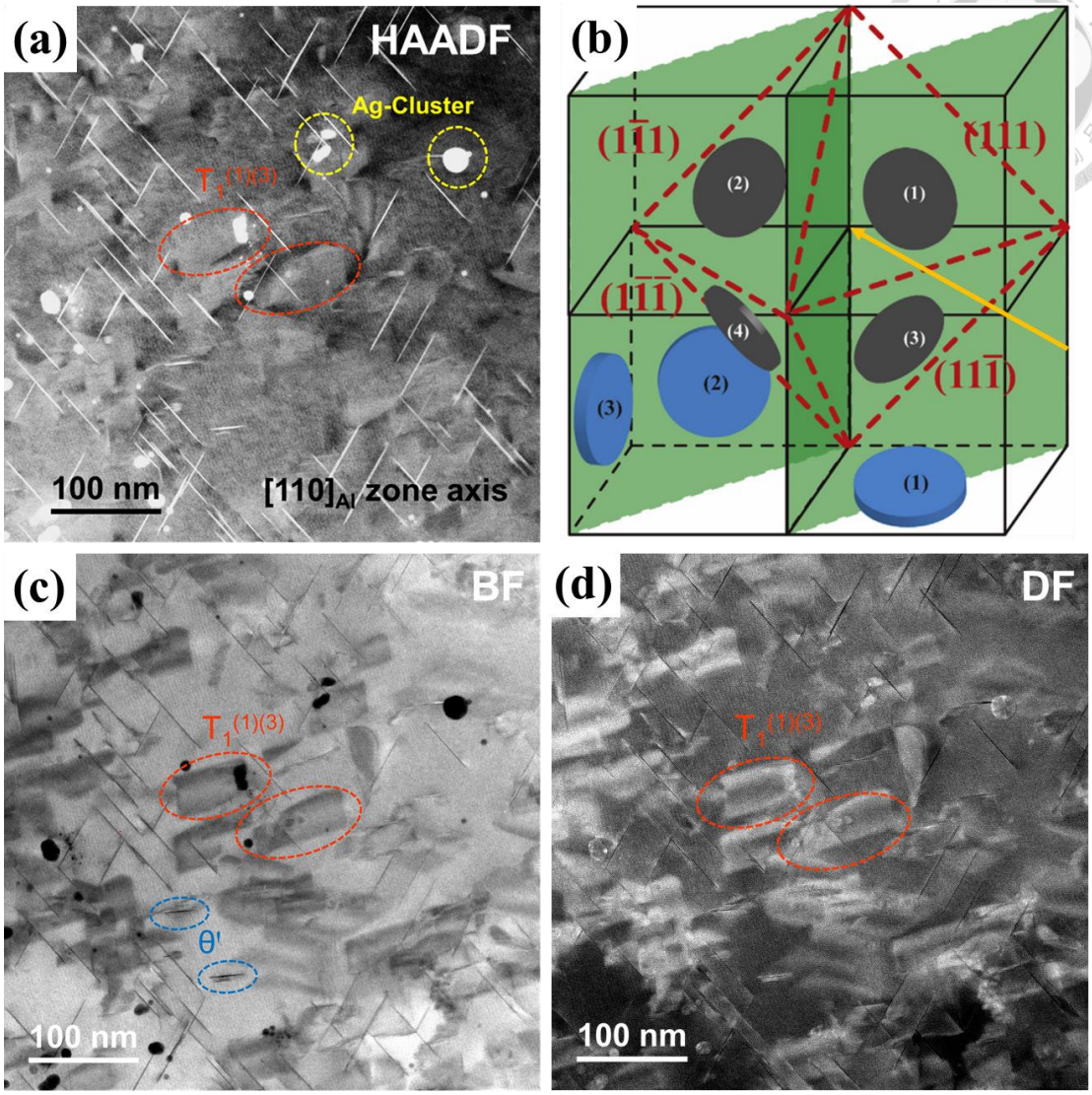

Figure 4-7 (a) HAADF-STEM, (c) BF-STEM, and (d) DF-STEM images of PA20 along the $[110]_{Al}$ zone axis

doi:10.6342/NTU202402902

4.2.4 Heterogeneous Nucleation of T_1 in PA20

This section discusses the heterogeneous nucleation phenomena at PA20, excluding dislocations. These include second-phase boundary and grain boundary. As shown in Figure 4-8a, such coarse second phases frequently exist in the aluminum alloy matrix. The boundary between the second phase and the matrix often shows white contrast due to precipitates decorating it. Magnified boundary images, as shown in Figure 4-8b, reveal many GP(T) and T_1 precipitates at the boundary, establishing another type of heterogeneous nucleation phenomenon.

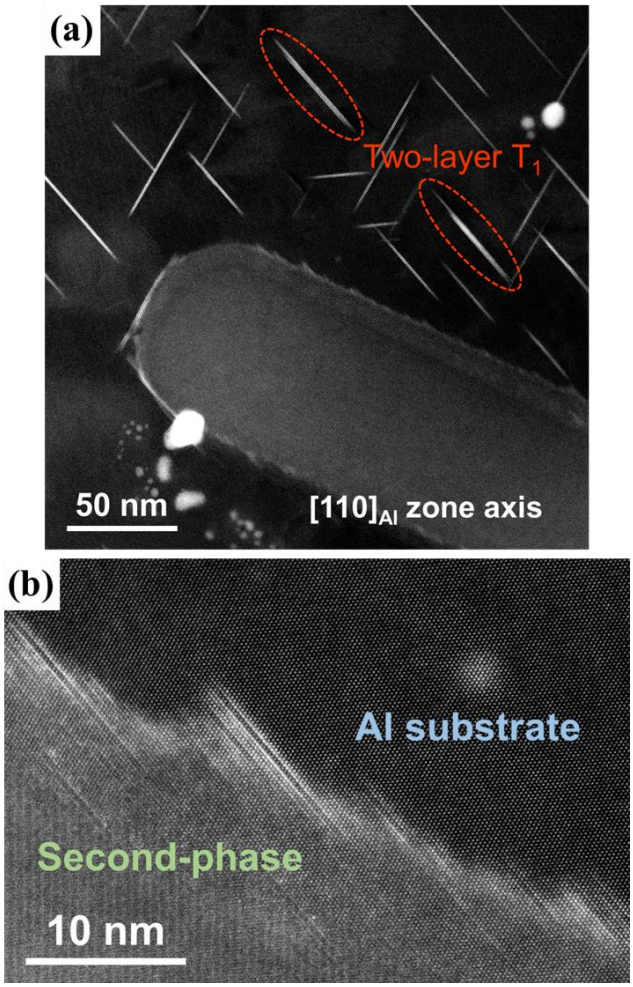

Figure 4-8 HAADF-STEM image of (a) the region surrounding the second phase along the $[110]_{Al}$ zone axis (b) the boundary between the second phase and the Al substrate

doi:10.6342/NTU202402902

Grain boundary precipitates are particularly significant. As shown in Figure 4-9a, numerous coarse and short T_1 precipitates can be found at the grain boundaries. This solute segregation at the grain boundaries also leads to the formation of a precipitation-free zone (PFZ), which negatively affects both mechanical and corrosion properties. Figure 4-9b shows an atomic-scale image of grain boundary T_1 precipitates, displaying a unique eight-layer structure, differing from the common one-layer or two-layer structures, indicating a higher heterogeneous nucleation capability at grain boundaries compared to dislocations and second phases.

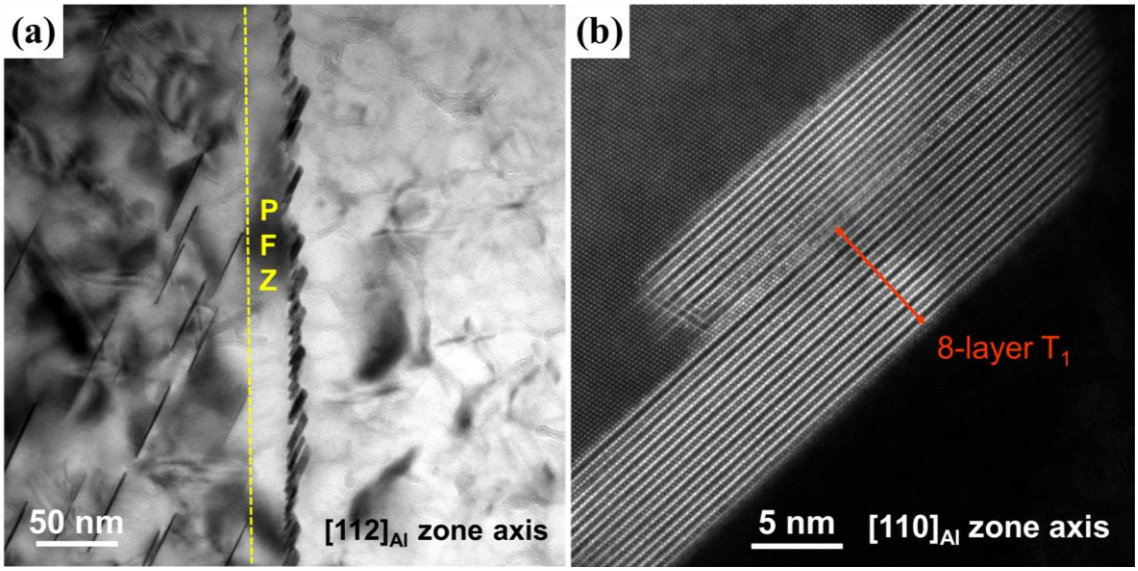

Figure 4-9 (a) BF-TEM image of grain boundary precipitates and PFZ, and (b) HAADF-STEM image of an 8-layer T_1 precipitate on the grain boundary.

doi:10.6342/NTU202402902

4.3 Pre-Strain Creep Aging

4.3.1 Pre-Strain Creep Aging 20 Hours (PCA20)

After pre-straining, the material underwent creep aging at 155°C for 20 hours under a stress of 175 MPa. The TEM bright-field images, as shown in Figure 4-10, indicate that the size of T_1 precipitates is similar to that observed in PA20. The selected area diffraction pattern in the upper right corner of Figure 4-10 indicates that T_1 is the predominant precipitate.

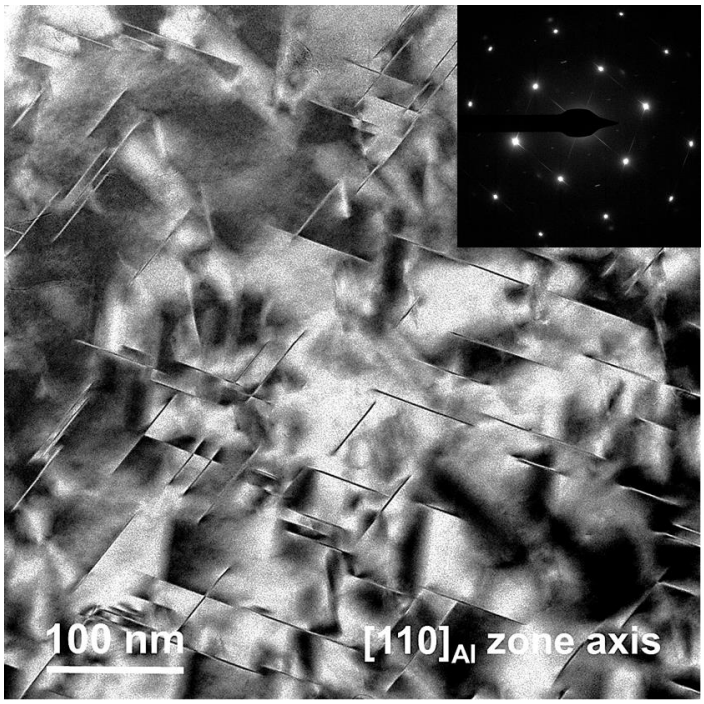

Figure 4-10 TEM BF image of PCA20 process along the $[110]_{Al}$ zone axis

doi:10.6342/NTU202402902

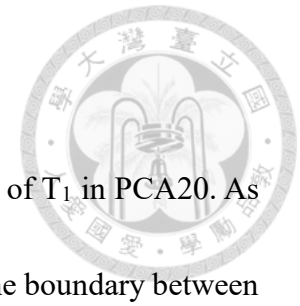

4.3.2 Heterogeneous Nucleation of T_1 in PCA20

This section continues to explore the heterogeneous nucleation of T_1 in PCA20. As shown in Figure 4-11, numerous T_1 precipitates can be observed at the boundary between the second phase and the matrix. EDS analysis, shown in Figures 4-11b and 4-11d, indicates that the second phase mainly consists of Mn and Cu elements, while the presence of Cu in the T_1 composition is also evident. Additionally, elements such as Ag and Mg, which often segregate around T_1, can be seen surrounding the second phase boundary, indicating that T_1 heterogeneous nucleation occurs at the second phase-matrix boundary. Moreover, Ag-clusters are occasionally observed in the aluminum matrix, though this phenomenon has not been deeply studied.

Grain boundary precipitation phenomena show notable changes. Figure 4-12a demonstrates that coarse T_1 precipitates are still present at the grain boundaries, but the PFZ is less pronounced compared to PA20. Based on EDS data, solute elements tend to segregate at the grain boundaries, but as observed in Figure 4-12c, the segregation of Cu does not clearly indicate a PFZ, showing a difference from PA20.

doi:10.6342/NTU202402902

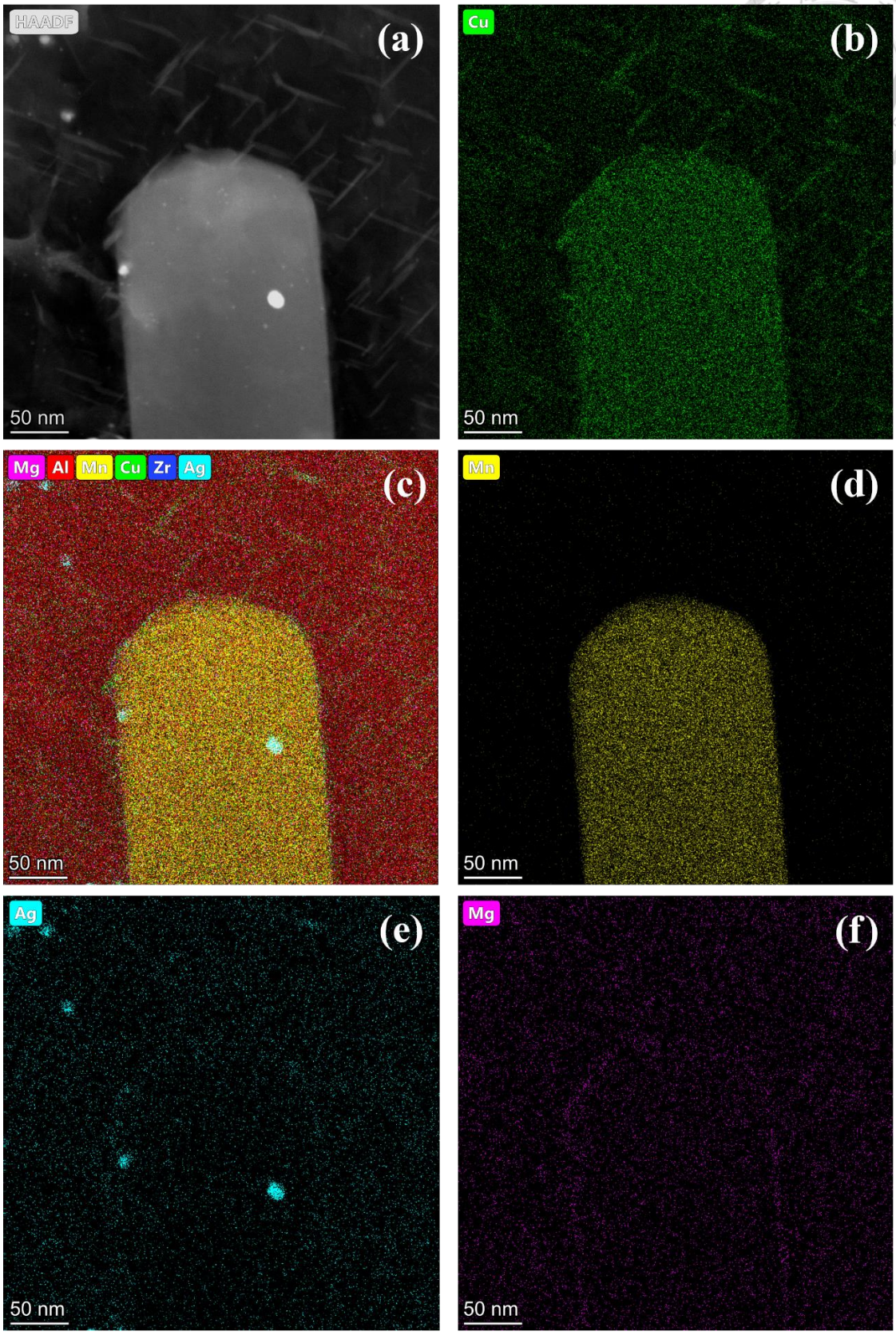

Figure 4-11 (a) HAADF-STEM image of the region surrounding the second phase along the $[110]_{Al}$ zone axis (b-f) STEM EDX mapping

doi:10.6342/NTU202402902

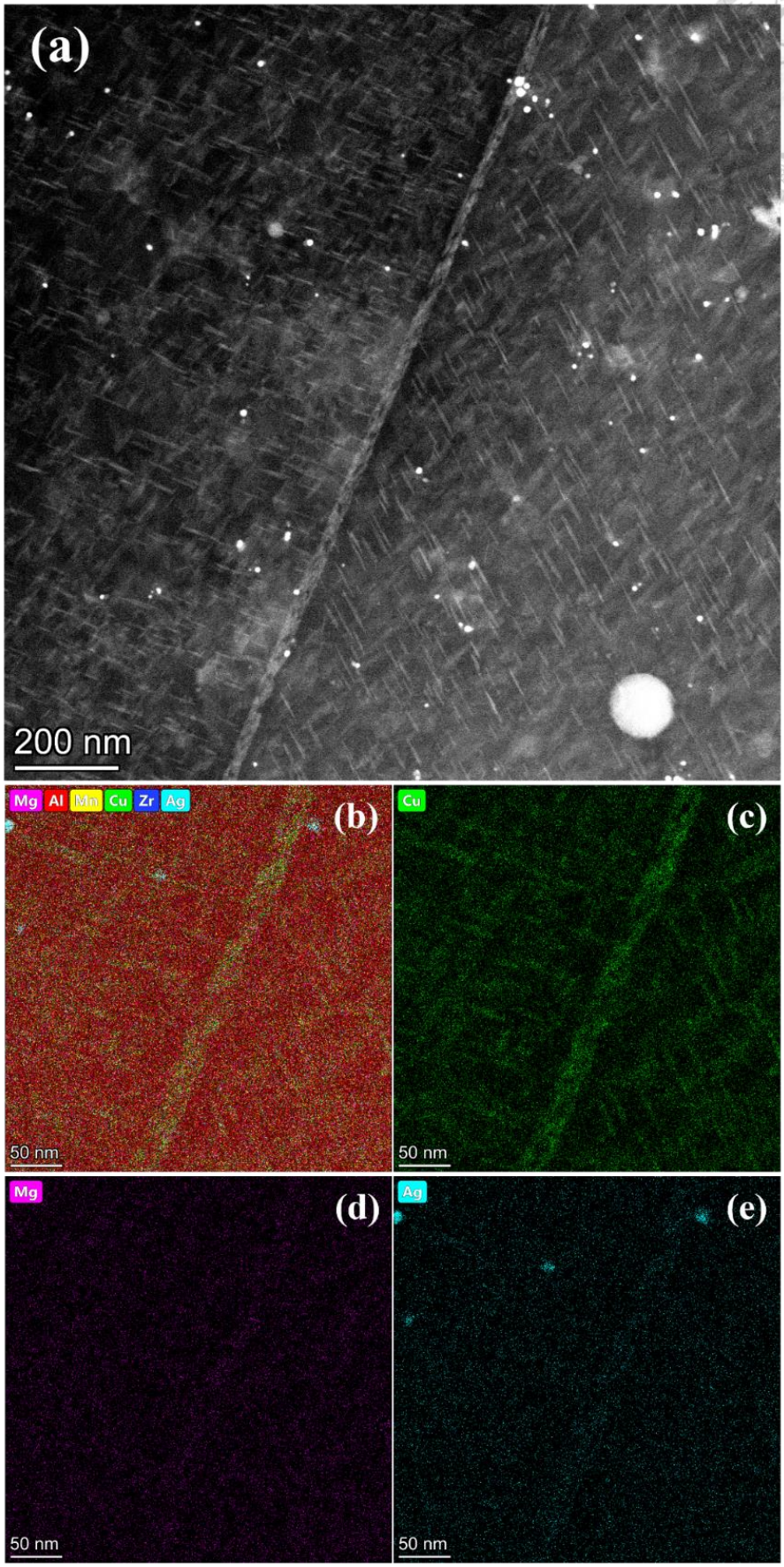

Figure 4-12 (a) HAADF-STEM image of the region surrounding the grain boundary along the $[110]_{Al}$ zone axis (b-e) STEM EDX mapping

doi:10.6342/NTU202402902

4.4 T_1 Precipitates Size and Volume Fraction

4.4.1 TEM

This section collects TEM images from the previous aging parameter studies and measures the diameter of over 100 T_1 precipitates. The data are presented in Figure 4-13 and Table 4-2, showing that the diameter of T_1 increases with aging time. At PA20, the diameter is approximately 47.6 nm, while at PCA20, it is around 49.8 nm. However, the standard deviation is large, indicating no statistical difference. SAXS data can provide more precise measurements. Although it is challenging to determine T_1 thickness from low-magnification images, atomic-scale images show that most T_1 precipitates in the matrix are single-layered, with a thickness of 1.3 nm, occasionally forming two-layer or three-layer structures, as indicated in Figure 4-8.

Table 4-2 Average T_1 precipitate diameter for different aging periods by TEM

Aging Period	PA4	PA8	PA14	PA20	PCA20
T_1 Diameter (nm)	21.6±8.5	34.6±16.3	40.3±18.3	47.6±17.1	49.8±18.55

doi:10.6342/NTU202402902

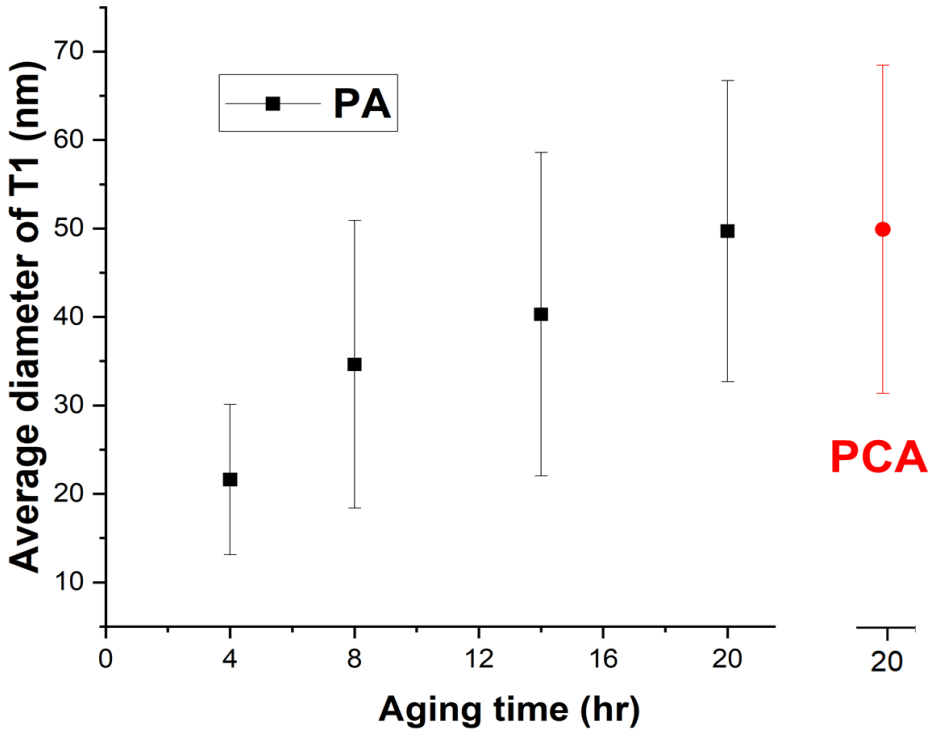

Figure 4-13 Average T_1 precipitate diameter for different aging periods by TEM

4.4.2 SAXS

SAXS measurements were conducted for PA4, PA14, PA20, and PCA20 parameters. Figures 4-14 and 4-15 show the 2D patterns, which were processed to obtain one-dimensional data of scattering intensity I(q) versus scattering vector q. These data were fitted using a cylinder form function in SAXSview to derive information on the diameter, thickness, and relative volume fraction of T_1, as presented in Tables 4-3 and 4-4.

Notably, the T_1 size in PA20 is longer and thinner compared to PCA20, although the difference is not substantial. From PA4 to PA20, the volume fraction of precipitates continuously increases. Additionally, the volume fraction in PCA20 is 11% greater than that in PA20.

doi:10.6342/NTU202402902

Table 4-3 T_1 precipitate diameter and thickness for PA20 and PCA20 by SAXS

Sample	PA20	PCA20
T_1 diameter (nm)	57.5	49.3
T_1 thickness (nm)	1.38	1.67

Table 4-4 Relative volume fraction of T_1 for different sample

Sample	PA4	PA14	PA20	PCA20
Relative volume fraction	0.44	0.66	1	1.11

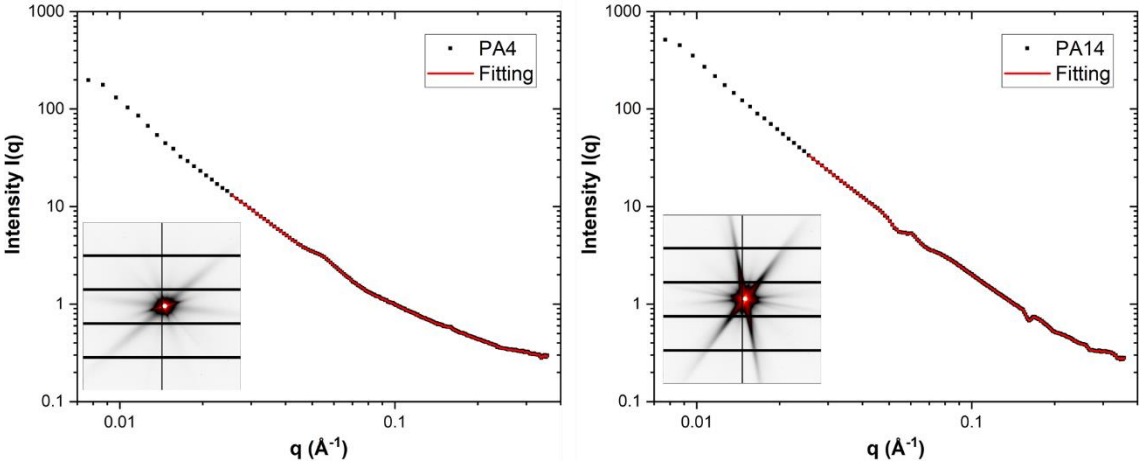

Figure 4-14 SAXS 2D patterns and I(q) versus q curves for PA4 and PA14 sample

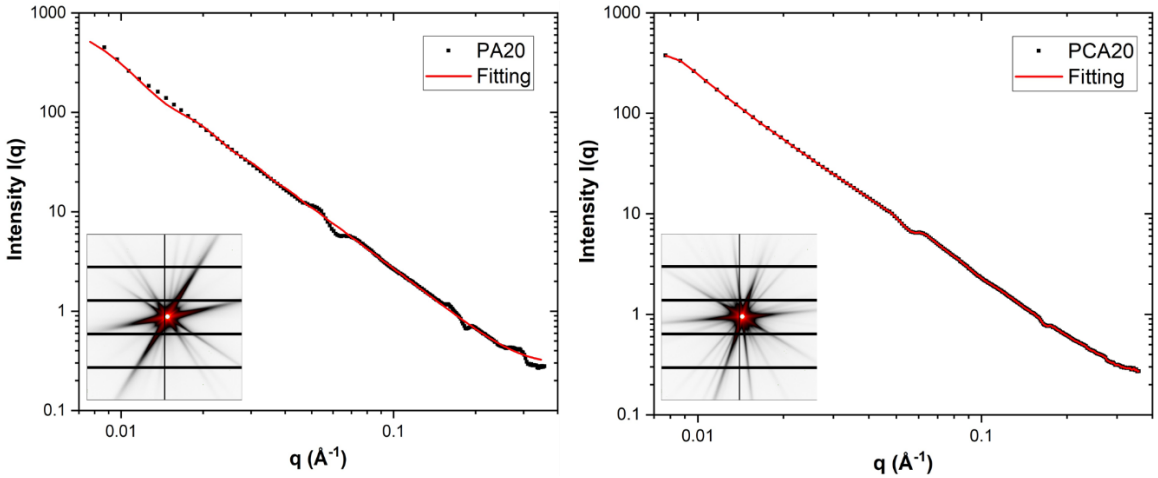

Figure 4-15 SAXS 2D patterns and I(q) versus q curves for PA20 and PCA20 sample

doi:10.6342/NTU202402902

4.5 Mechanical Property

Hardness tests were conducted on samples aged with PA and PCA parameters, as shown in Figure 4-16. Notably, PCA20 exhibited a hardness of 172.4 HV, 10.1 HV higher than PA20's 162.3 HV. Tensile tests for PCA20 and PA20 revealed that PCA20 had a YS of 510.5 MPa, 20.3 MPa higher than PA20's 490.2 MPa, indicating that PCA resulted in higher strength without reducing ductility.

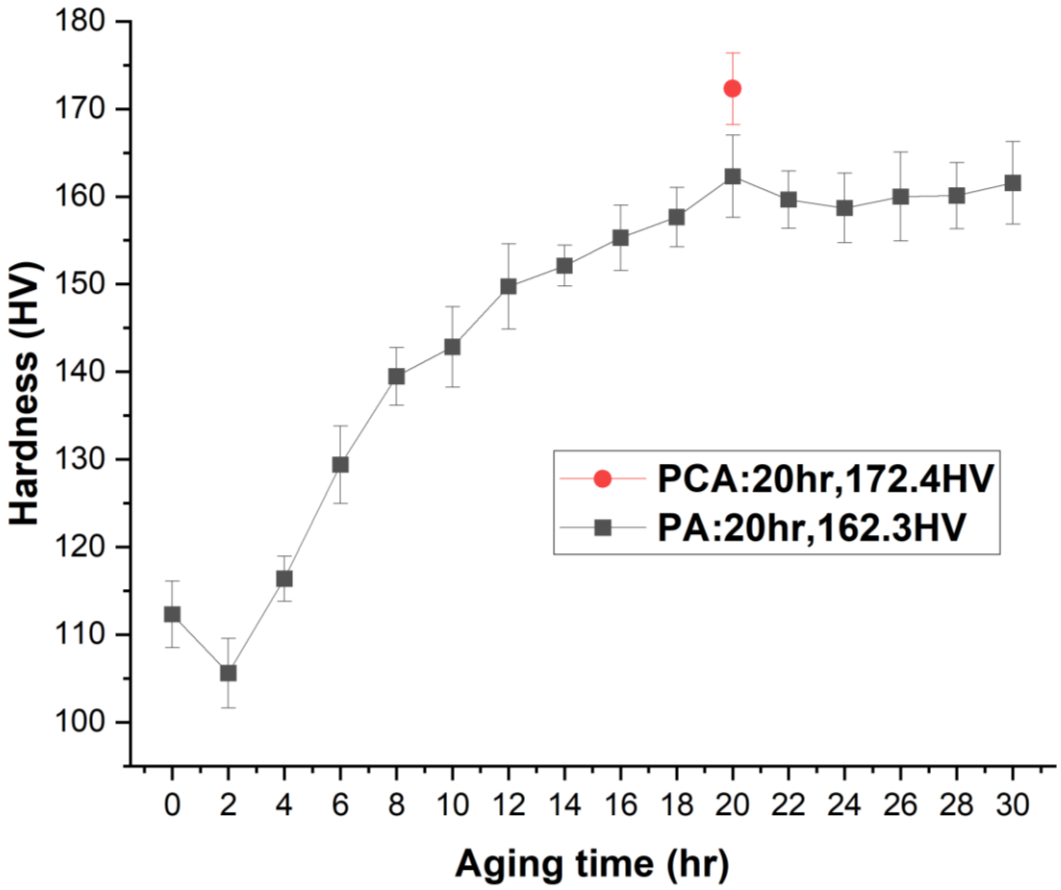

Figure 4-16 Hardness results of PA20 and PCA20 specimen

doi:10.6342/NTU202402902

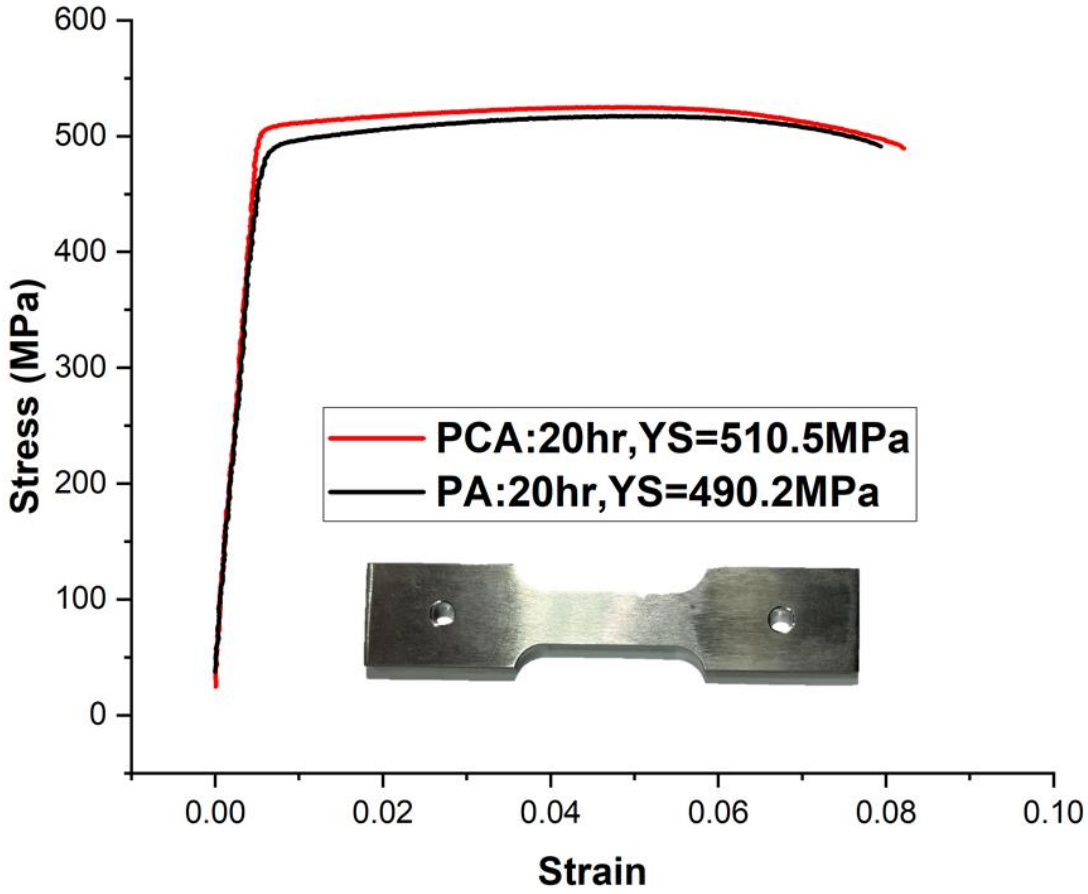

Figure 4-17 Tensile results of PA20 and PCA20 specimen

4.6 Summary

In summary, the study demonstrated that following solution heat treatment (SHT), applying PA and PCA promoted the growth of precipitates with increasing aging time, reaching an optimal size at peak aging (20 hours). There was no significant difference in the types of precipitates within the matrix between PA and PCA, but PCA exhibited smaller precipitate-free zones (PFZs) around grain boundaries. This is attributed to dislocations introduced during creep aging, which promoted T1 precipitation more within the matrix, leaving fewer solutes to precipitate at grain boundaries. Literature suggests

doi:10.6342/NTU202402902

that smaller PFZs enhance fracture toughness, potentially explaining PCA's better ductility compared to PA.

SAXS analysis indicated that PCA20 had a higher volume fraction of precipitates compared to PA20 and suggested that the dislocation density of PCA20 was higher than that of PA20. The relationship between YS, dislocations, and precipitates can be derived from the following formula:

$$\sigma_y = M(\tau_B + \Delta\tau_\rho + \Delta\tau_P)$$

Where σ_y is the yield strength of the material, τ_B is the constant matrix shear strength, $\Delta\tau_\rho$ and $\Delta\tau_P$ are the strengths increased due to dislocation and precipitation, respectively, and M is the Taylor factor. The contributions of dislocations and precipitates are higher in PCA20 than in PA20, indicating that PCA20 has higher yield strength.

doi:10.6342/NTU202402902

Chapter 5 Results of Atomic-Scale Investigation of T_1 Precipitates

5.1 GP(T_1) and T_1

In this section, we introduce the methods to identify GP(T_1) and T_1 precipitates at the atomic scale, discuss the transformation process, and explain the thickening mechanism of T_1 precipitates.

5.1.1 Identifying GP(T_1) and T_1

At low magnification, it is difficult to distinguish between GP(T_1) and T_1 precipitates, as illustrated in Figure 5-1a. Both types of precipitates on the {111} plane appear almost identical. However, at higher magnification with clear atomic-scale imaging, their differences become apparent, as shown in Figure 5-1b.

Firstly, the mid-layer of the GP(T_1) precipitate, located at the bottom, exhibits contrast, unlike the completely dark mid-layer of the T_1 structure. This difference is due to the mid-layer of T_1 being occupied entirely by Li atoms, which are not captured in HAADF images. Secondly, GP(T_1) is fully coherent with the matrix, indicated by the absence of lattice distortion in the yellow lines, while T_1 causes lattice distortion, causing the yellow lines to shift slightly.

doi:10.6342/NTU202402902

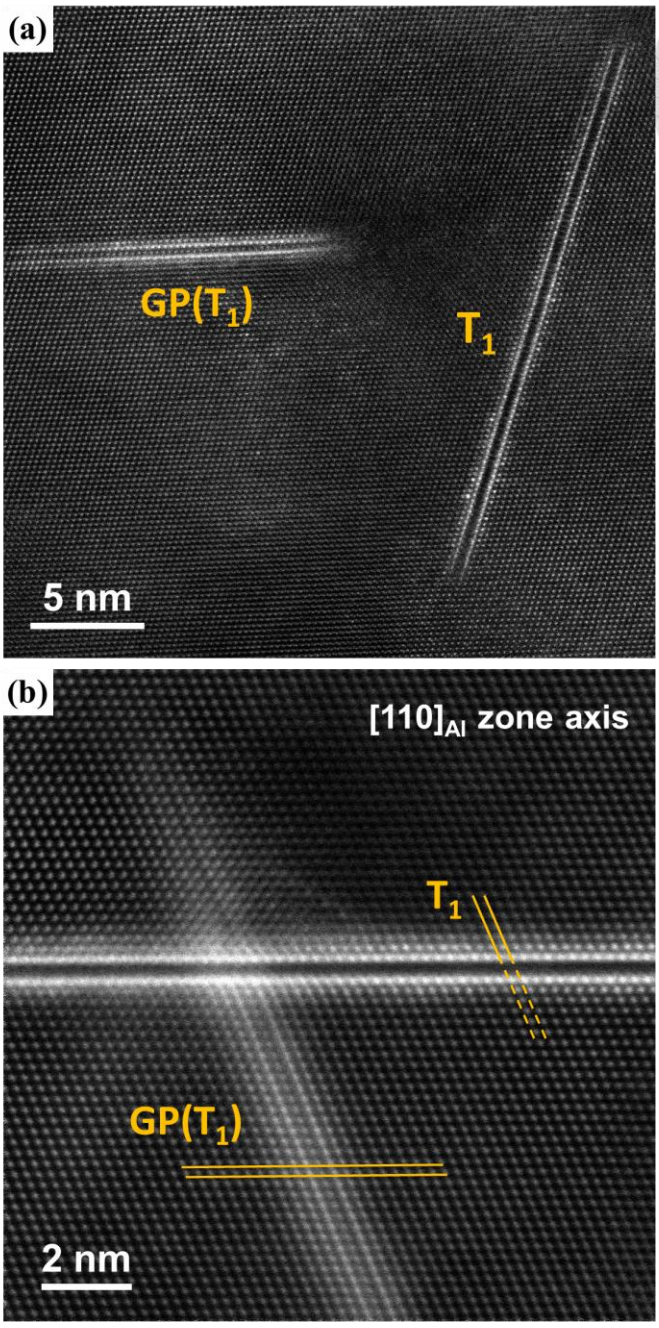

Figure 5-1 HR-STEM images of GP(T_1) and T_1 precipitate along the $[110]_{Al}$ zone axis

5.1.2 In-situ Transformation

The transformation from GP(T_1) to T_1 occurs via in-situ transformation, as shown in Figure 5-2a. The GP(T_1) precipitate, enclosed by a yellow box, shows slight contrast in the mid-layer, while the right end of the same precipitate is T_1. This transformation is

doi:10.6342/NTU202402902

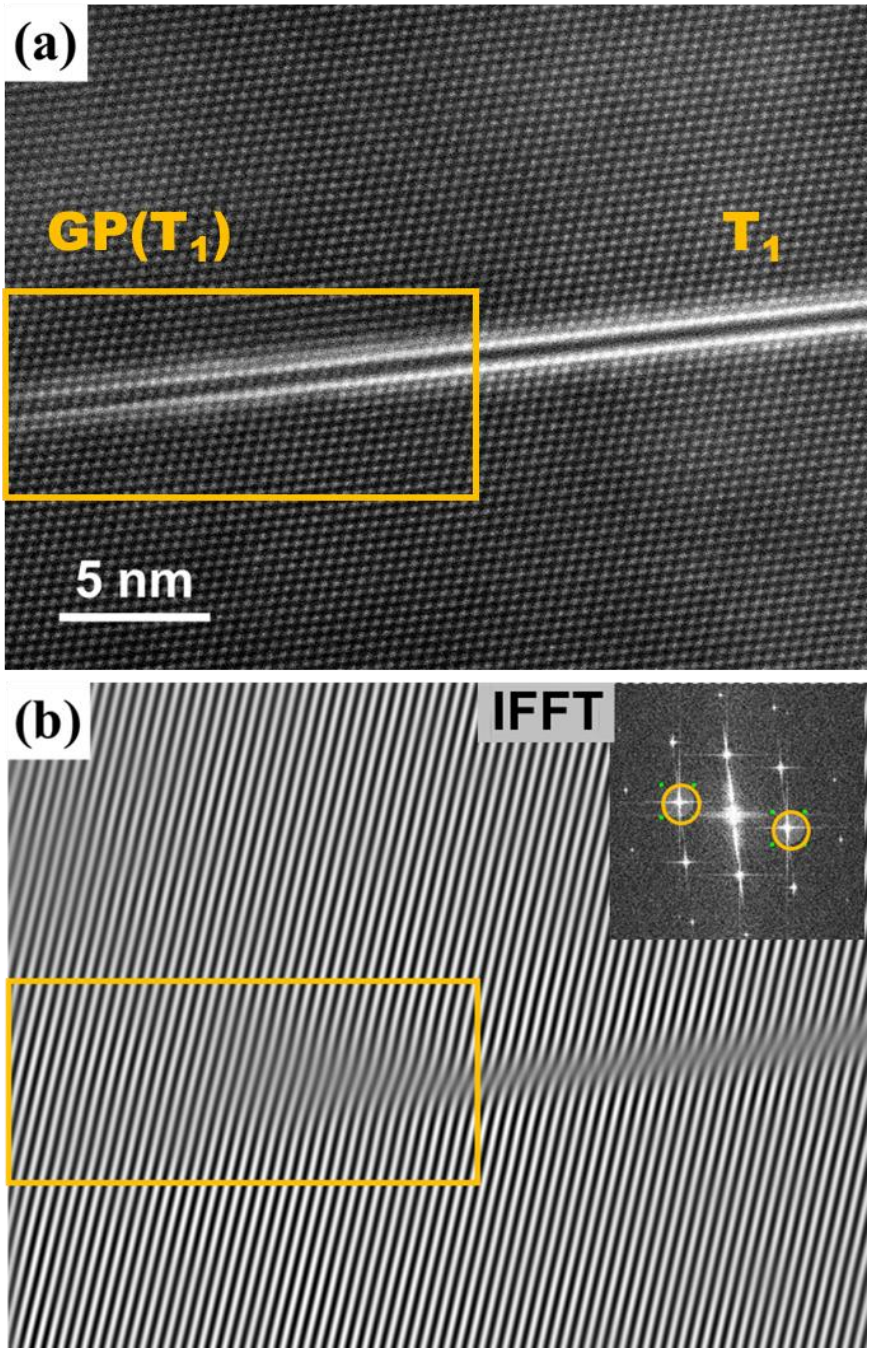

Figure 5-2 (a) HR-STEM image of GP(T_1) in-situ transforming into T_1 precipitate along the $[110]_{Al}$ zone axis (b) IFFT fringe image generated from the masked spots of the matrix

doi:10.6342/NTU202402902

5.2 Coarsening Morphology

During heat treatment, T_1 precipitates are observed to thicken, as illustrated in Figure 5-3a. The thickening mechanism involves the growth of a GP(T_1) precipitate adjacent to a one-layer T_1, which then gradually transforms into a two-layer T_1. Figure 5-3b shows a two-layer T_1 transforming into a three-layer T_1, a common lateral growth mechanism.

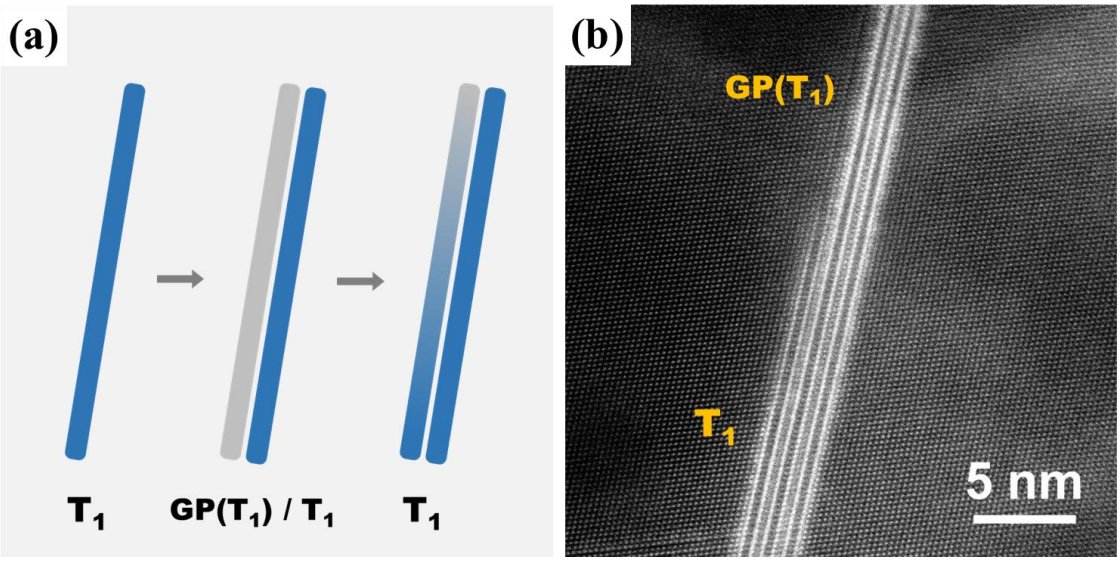

Figure 5-3 (a) Schematic diagram of T_1 thickening (b) HR-STEM image of a 2-layer T_1 in-situ transforming into a 3-layer T_1 precipitate along the $[110]_{Al}$ zone axis

A unique two-layer T_1 structure was identified, as shown in Figure 5-4a. This T_1 precipitate, larger than 56nm, displays a central piercing morphology in the second layer. At higher magnification in Figure 5-4b, it is evident that the upper part thickens via a type-II mechanism, while the lower part thickens via a type-I mechanism. It is hypothesized that the upper part of this long T_1 precipitate grows through the type-II

doi:10.6342/NTU202402902

thickening mechanism, and the lower part through the type-I mechanism, colliding later to form this unique morphology.

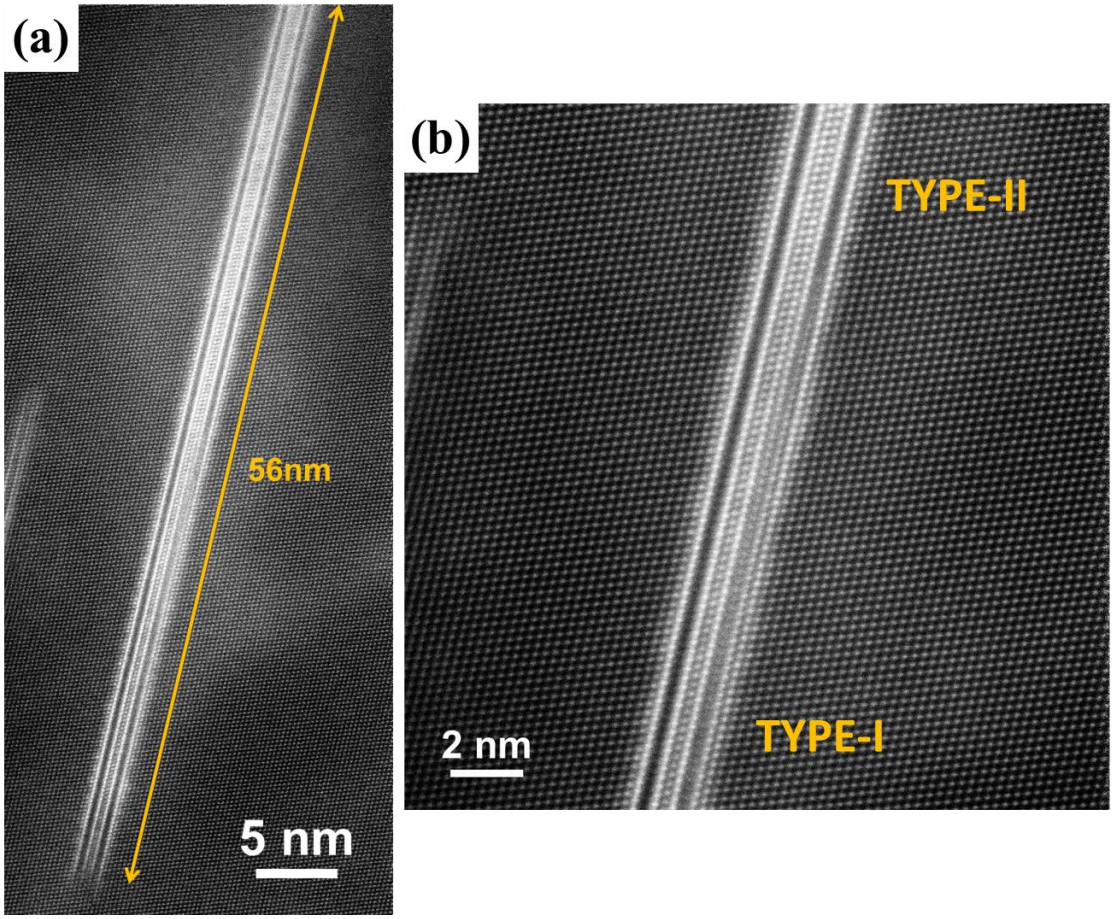

Figure 5-4 (a) HR-STEM image of special T_1 (b) HR-STEM image of TYPE-I thickening T_1 colliding with TYPE-II T_1 precipitate along the $[110]_{Al}$ zone axis

doi:10.6342/NTU202402902

5.3 Shearing Morphology

Observations were made on PA20 samples subjected to tensile testing until fracture. Numerous dislocations were found to have cut through the precipitates, leaving traces, as shown in Figure 5-5a. Using the [110] zone axis, two parallel {111} planes can be observed, allowing us to see dislocations on the (1-11) plane cutting through precipitates on the (-111) plane. The dislocation cutting angle is 70.52 degrees, providing further evidence of this mechanism. However, using the [112] zone axis, the cutting angle of the precipitate by dislocations is not parallel to the observation direction, resulting in overlapping images.

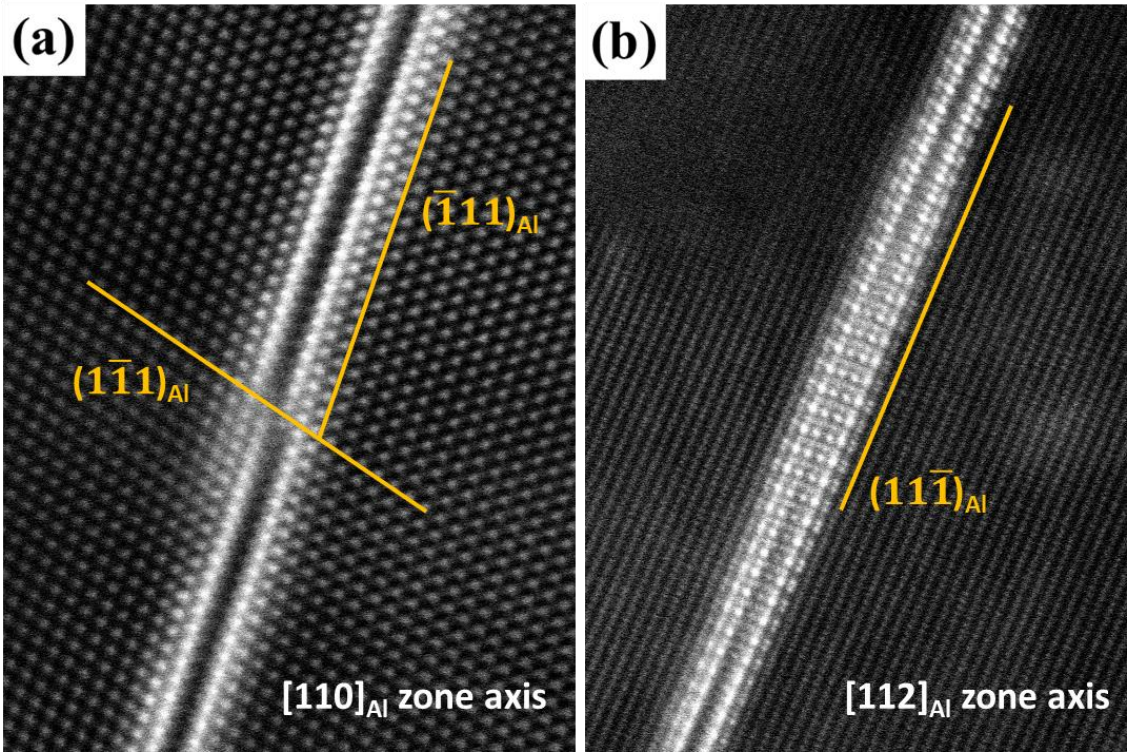

Figure 5-5 HR-STEM image of shearing morphologies along the (a) $[110]_{Al}$ zone axis (b) $[112]_{Al}$ zone axis

doi:10.6342/NTU202402902

5.4 IDPC-STEM

HAADF-STEM imaging cannot capture the contrast of Li atoms, leading to only a preliminary understanding of the T_1 precipitate mechanism. Improved imaging techniques could provide deeper insights. Figure 5-6a shows the most widely used atomic structure model of T_1, indicating that the mid-layer consists entirely of Li. Figure 5-6b shows a HAADF image of T_1, where the mid-layer appears entirely black, with the simulated HAADF image in the lower right corner confirming that even in ideal conditions, light elements like Li cannot be observed.

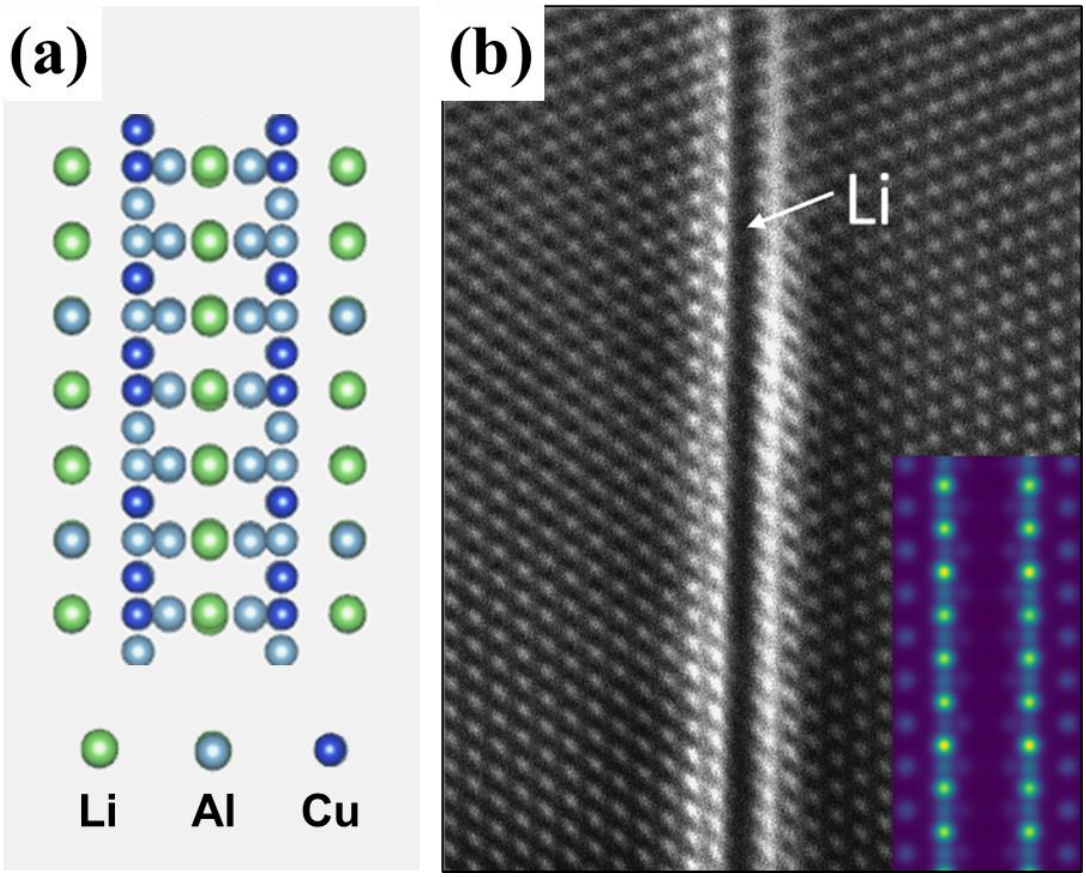

Figure 5-6 (a) Atomic structure of T_1 [38] (b) HR-STEM and simulation images of T_1 precipitate along the $[110]_{Al}$ zone axis

doi:10.6342/NTU202402902

The invention of IDPC-STEM allows simultaneous imaging of both light and heavy elements. The IDPC image of a T_1 precipitate in Figure 5-7 clearly captures the Li elements in the mid-layer, and other layers, which are less clear in HAADF images, are also more distinctly visible. Comparing the model with the image confirms all atomic points, further validating the accuracy of the model and providing a new method to explore the T_1 mechanism in greater depth.

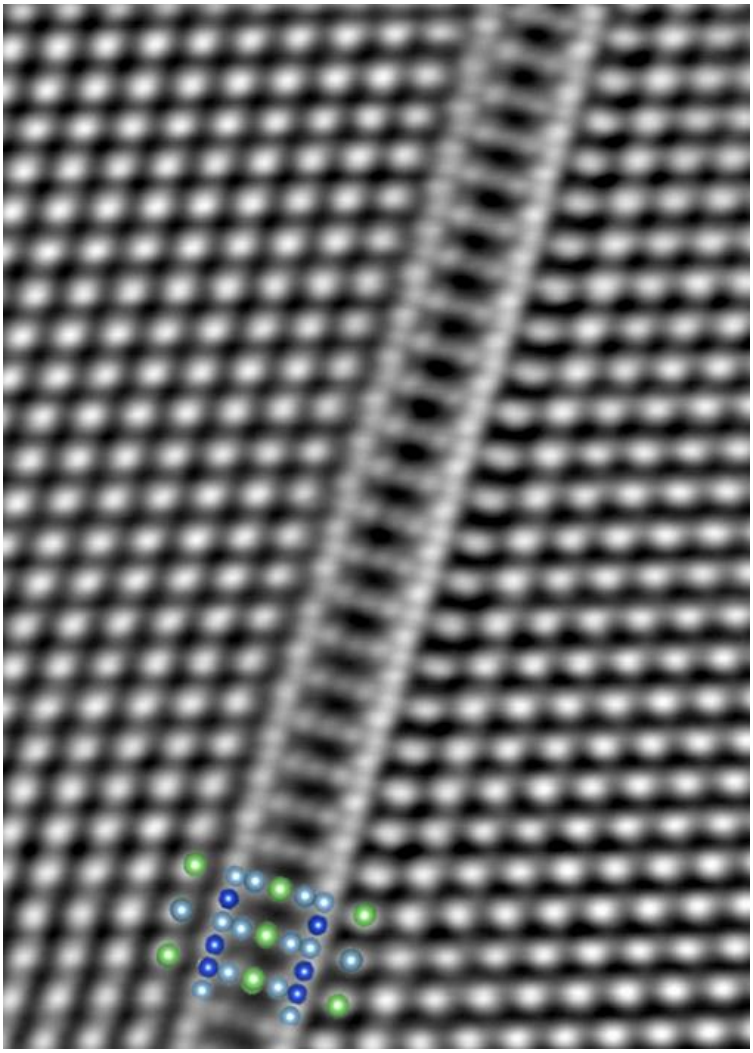

Figure 5-7 iDPC-STEM image of T_1 precipitate along the $[110]_{Al}$ zone axis

doi:10.6342/NTU202402902

Chapter 6 Highlights

1. Pre-strain aging for 20 hours (PA20) reaches the peak aging stage, where the precipitates grow to their optimal size, and the mechanical properties of the material achieve their maximum values.
2. T_1 precipitates predominantly nucleate heterogeneously on dislocations, secondary phases, and grain boundaries. The former two are mostly 1-layer T_1 precipitates, while the grain boundaries exhibit coarser 8-layer T_1 precipitates.
3. Pre-strain Creep Aging for 20 hours (PCA20) results in a smaller precipitation-free zone near the grain boundaries compared to PA20.
4. Hardness of PCA20 increases by 10.1 HV, and the yield strength (YS) improves by 20.3 MPa compared to PA20.
5. T_1 precipitate size analysis shows a good agreement between TEM and SAXS data. SAXS data indicates that the precipitates in PA20 are longer and thinner, while those in PCA20 are shorter and thicker.
6. Distinguishing between GP(T_1) and T_1 precipitates requires atomic-scale imaging. This study also provides in-situ transformation images that demonstrate the transition from coherent to incoherent structures.
7. For the first time, this study identifies a collision mechanism (TYPE-I and TYPE-II) during the thickening of T_1 precipitates.

doi:10.6342/NTU202402902

8. T_1 iDPC-STEM images were captured for the first time, clearly showing the positions of Li elements, highlighting significant potential for future research into more detailed mechanisms.

doi:10.6342/NTU202402902

Chapter 7 Future Works

- **Quantification of T_1 precipitate density around grain boundaries**

  Although previous research has indicated that the PFZ near grain boundaries is relatively small for PCA20, further quantitative data is needed to ensure the rigor of the experiments. EELS must be used to measure the specimen thickness, which is essential for quantifying the precipitates around the grain boundaries.

- **More T_1 IDPC imaging**

  With the capability of IDPC imaging to capture Li atoms, we can delve deeper into the T_1 cutting mechanism, including determining which plane of the precipitate is being cut. Additionally, capturing in-situ transformation images from GP(T_1) to T_1 using IDPC will provide insights into the distribution of Li within the T_1 precipitates.

- **Atomic EDS of T_1**

  Using Atomic Energy Dispersive Spectroscopy (EDS) to collect signals of Mg, Ag, and Mn will enable a deeper understanding of the segregation of trace elements in T_1. This analysis will offer a more comprehensive insight into the role of these elements in the microstructural evolution and stability of T_1 precipitates.

doi:10.6342/NTU202402902

Appendix A: Specimen Explosion

During the 500°C Solution Heat Treatment, an incident occurred where a specimen exploded in the high-temperature furnace. It is hypothesized that the explosion was caused by the oxidation reaction of Li elements within the material at high temperatures. Figure A-1 shows the specimen before and after the explosion. After the explosion, the specimen's surface became rough and exhibited small holes, losing its metallic luster.

Subsequently, both the normal specimen and the exploded specimen were sent for compositional analysis using an ICP-MS instrument. The analysis results are presented in Table A-1. It was found that the Li content in the exploded specimen had decreased, further confirming that the explosion was caused by the oxidation of Li elements.

Therefore, for future Solution Heat Treatment (SHT) of Al-Cu-Li alloys, it may be advisable to use vacuum sealing to prevent such occurrences.

Table A-1 Composition comparison of explosive and normal samples (wt%)

Element	**Al**	**Cu**	**Li**	**Mg**	**Ag**
Normal Sample	Bal.	3.54	**0.98**	0.37	0.37
Explosive Sample	Bal.	3.55	**0.41**	0.14	0.15

doi:10.6342/NTU202402902

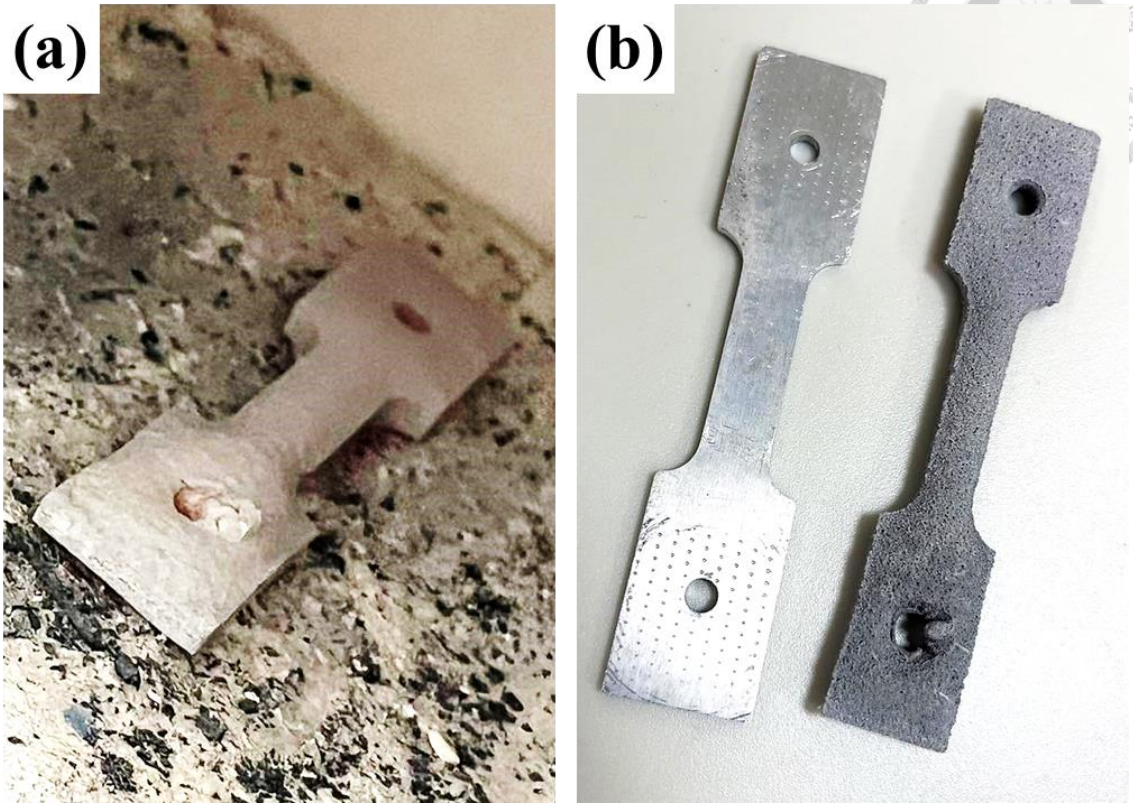

Figure A-1 (a) Explosive specimen in the high-temperature furnace (b) Comparison between normal and explosive specimens

doi:10.6342/NTU202402902

REFERENCE

[1] J.J. Rino, D. Chandramohan, K. Sucitharan, V.D. Jebin, An overview on development of aluminium metal matrix composites with hybrid reinforcement, Int. J. Sci. Res 1(3) (2012) 2319-7064.
[2] J.M. Runge, A Brief History of Aluminum and Its Alloys, in: J.M. Runge (Ed.), The Metallurgy of Anodizing Aluminum: Connecting Science to Practice, Springer International Publishing, Cham, 2018, pp. 1-63.
[3] G.E. Totten, D.S. MacKenzie, Handbook of aluminum: vol. 1: physical metallurgy and processes, CRC press2003.
[4] I. Polmear, D. StJohn, J.-F. Nie, M. Qian, Light alloys: metallurgy of the light metals, Butterworth-Heinemann2017.
[5] D. Ashkenazi, How aluminum changed the world: A metallurgical revolution through technological and cultural perspectives, Technological Forecasting and Social Change 143 (2019) 101-113.
[6] R.S. Long, E. Boettcher, D. Crawford, Current and Future Uses of Aluminum in the Automotive Industry, JOM 69(12) (2017) 2635-2639.
[7] E.A. Starke Jr, J.T. Staley, Application of modern aluminum alloys to aircraft, Progress in aerospace sciences 32(2-3) (1996) 131-172.
[8] M.C. Santos, A.R. Machado, W.F. Sales, M.A. Barrozo, E.O. Ezugwu, Machining of aluminum alloys: a review, The International Journal of Advanced Manufacturing Technology 86 (2016) 3067-3080.
[9] F.M. Mazzolani, Competing issues for aluminium alloys in structural engineering, Progress in Structural Engineering and Materials 6(4) (2004) 185-196.
[10] J.G. Kaufman, Introduction to aluminum alloys and tempers, ASM international2000.
[11] J.C. Benedyk, International temper designation systems for wrought aluminum alloys, Light metal age 67 (2010) 3-6.
[12] E.A. Starke, Historical Development and Present Status of Aluminum–Lithium Alloys, Aluminum-lithium Alloys2014, pp. 3-26.
[13] The Influence of Grain Structure on the Ductility of the Al-Cu-Li-Mn-Cd Alloy 2020, (1982).
[14] Review Aluminium-lithium alloys, (1987).
[15] J. Pickens, F. Heubaum, T. Langan, L. Kramer, Al-(4.5-6.3) Cu-1.3 Li-0.4 Ag-0.4 Mg-0.14 Zr alloy weldalite 049, Proceedings of the Fifth International Conference on Aluminum-Lithium Alloys. Birmingham: Materials and Component Engineering Publications Ltd, 1989, pp. 1397-1411.
[16] A. Abd El-Aty, Y. Xu, X. Guo, S.H. Zhang, Y. Ma, D. Chen, Strengthening mechanisms, deformation behavior, and anisotropic mechanical properties of Al-Li alloys:

doi:10.6342/NTU202402902

A review, J Adv Res 10 (2018) 49-67.
[17] J. Ma, X. Liu, D. Yan, L. Rong, A novel GP-Li precursor and the correlated precipitation behaviors in Al-Cu-Li alloys with different Cu/Li ratio, Acta Mater. 243 (2023) 118442.
[18] B. Decreus, A. Deschamps, F. De Geuser, P. Donnadieu, C. Sigli, M. Weyland, The influence of Cu/Li ratio on precipitation in Al–Cu–Li–x alloys, Acta Mater. 61(6) (2013) 2207-2218.
[19] E. Lavernia, T.S. Srivatsan, F. Mohamed, Strength, deformation, fracture behaviour and ductility of aluminium-lithium alloys, Journal of Materials Science 25 (1990) 1137-1158.
[20] E. Gumbmann, W. Lefebvre, F. De Geuser, C. Sigli, A. Deschamps, The effect of minor solute additions on the precipitation path of an Al Cu Li alloy, Acta Mater. 115 (2016) 104-114.
[21] E. Gumbmann, F. De Geuser, C. Sigli, A. Deschamps, Influence of Mg, Ag and Zn minor solute additions on the precipitation kinetics and strengthening of an Al-Cu-Li alloy, Acta Mater. 133 (2017) 172-185.
[22] A. Chen, L. Zhang, G. Wu, Y. Peng, Y. Li, Effect of Mn addition on microstructure and mechanical properties of cast Al–2Li–2Cu–0.8Mg–0.4Zn–0.2Zr alloy, Journal of Materials Research 31(2) (2016) 250-258.
[23] D. Tsivoulas, J.D. Robson, Heterogeneous Zr solute segregation and Al3Zr dispersoid distributions in Al–Cu–Li alloys, Acta Mater. 93 (2015) 73-86.
[24] A. Guinier, Structure of age-hardened aluminium-copper alloys, Nature 142(3595) (1938) 569-570.
[25] G. Preston, The diffraction of X-rays by age-hardening aluminium copper alloys, Proceedings of the Royal Society of London. Series A. Mathematical and Physical Sciences 167(931) (1938) 526-538.
[26] R. Nicholson, J. Nutting, Direct observation of the strain field produced by coherent precipitated particles in an age-hardened alloy, The Philosophical Magazine: A Journal of Theoretical Experimental and Applied Physics 3(29) (1958) 531-535.
[27] Y. Chang, Crystal Structure and Nucleation Behavior of (111) Precipitates in an Al-3.9 Cu-0.5 Mg-0.5 Ag Alloy, 1993.
[28] 鍾采甫, AA7050 (Al-Zn-Mg) 和 AA2050 (Al-Cu-Li) 鋁合金原子級析出物之演化, 材料科學與工程學研究所, 國立臺灣大學, 台北市, 2019, p. 239.
[29] T.-F. Chung, Y.-L. Yang, C.-N. Hsiao, W.-C. Li, B.-M. Huang, C.-S. Tsao, Z. Shi, J. Lin, P.E. Fischione, T. Ohmura, J.-R. Yang, Morphological evolution of GP zones and nanometer-sized precipitates in the AA2050 aluminium alloy, International Journal of Lightweight Materials and Manufacture 1(3) (2018) 142-156.
[30] Y. Deng, J. Bai, X. Wu, G. Huang, L. Cao, L. Huang, Investigation on formation mechanism of T1 precipitate in an Al-Cu-Li alloy, Journal of Alloys and Compounds 723

doi:10.6342/NTU202402902

(2017) 661-666.
[31] S.C. Wang, M.J. Starink, Precipitates and intermetallic phases in precipitation hardening Al-Cu-Mg-(Li) based alloys, International Materials Reviews 50(4) (2005) 193-215.
[32] R.A. Herring, F.W. Gayle, J.R. Pickens, High-resolution electron microscopy study of a high-copper variant of weldalite 049 and a high-strength AI-Cu-Ag-Mg-Zr alloy, Journal of Materials Science 28(1) (1993) 69-73.
[33] J.C.H.A.J. Ardell, Crystal structure and stability of T, precipitates in aged AI-Li-Cu alloys, (1987).
[34] J.L. J.M. HOWE, and A. K. VASUDI~VAN, Structure and Deformation Behavior of T1 Precipitate Plates in an AI-2Li-1Cu Alloy, (1988).
[35] A.M. S. VAN SMAALEN, AND J. L. DE BOER, Refinement of the Crystal Structure of Hexagonal AI2CuLi, (1990).
[36] P. Donnadieu, Y. Shao, F. De Geuser, G.A. Botton, S. Lazar, M. Cheynet, M. de Boissieu, A. Deschamps, Atomic structure of T1 precipitates in Al–Li–Cu alloys revisited with HAADF-STEM imaging and small-angle X-ray scattering, Acta Mater. 59(2) (2011) 462-472.
[37] C. Dwyer, M. Weyland, L.Y. Chang, B.C. Muddle, Combined electron beam imaging and ab initio modeling of T1 precipitates in Al–Li–Cu alloys, Applied Physics Letters 98(20) (2011).
[38] K. Kim, B.-C. Zhou, C. Wolverton, First-principles study of crystal structure and stability of T1 precipitates in Al-Li-Cu alloys, Acta Mater. 145 (2018) 337-346.
[39] B. Na, B.-C. Zhou, C. Wolverton, K. Kim, First-principles Calculations of Bulk and Interfacial Thermodynamic Properties of the T1 phase in Al-Cu-Li alloys, Scripta Materialia 202 (2021).
[40] L. Bourgeois, C. Dwyer, M. Weyland, J.-F. Nie, B.C. Muddle, Structure and energetics of the coherent interface between the θ' precipitate phase and aluminium in Al－Cu, Acta Mater. 59(18) (2011) 7043-7050.
[41] X. Zhao, W. Liu, D. Xiao, Y. Ma, L. Huang, Y. Tang, A critical review: Crystal structure, evolution and interaction mechanism with dislocations of nano precipitates in Al-Li alloys, Materials & Design 217 (2022).
[42] H. Djaaboube, D. Thabet-Khireddine, TEM diffraction study of Al2CuMg (S´/S) precipitation in an Al－Li－Cu－Mg(Zr) alloy, Philosophical Magazine 92(15) (2012) 1876-1889.
[43] Z. Gao, J.Z. Liu, J.H. Chen, S.Y. Duan, Z.R. Liu, W.Q. Ming, C.L. Wu, Formation mechanism of precipitate T1 in AlCuLi alloys, Journal of Alloys and Compounds 624 (2015) 22-26.
[44] Y. Feng, X. Chen, Y. Hao, X. Li, B. Chen, Coarsening mechanism of T1 precipitation and calculation of T1/Al interface properties in 2198 Al–Cu–Li alloys: Experimental and

doi:10.6342/NTU202402902

DFT studies, Vacuum 204 (2022).
[45] T. Gladman, Precipitation hardening in metals, Materials science and technology 15(1) (1999) 30-36.
[46] A.J. Ardell, Precipitation hardening, Metallurgical Transactions A 16(12) (1985) 2131-2165.
[47] Symposium on Internal Stresses in Metals and Alloys, Nature 164(4164) (1949) 296-296.
[48] B.C.M. J.F. Nie, On the form of the age-hardening response in high strength aluminium alloys, (2001).
[49] T. Dorin, A. Deschamps, F.D. Geuser, C. Sigli, Quantification and modelling of the microstructure/strength relationship by tailoring the morphological parameters of the T1 phase in an Al–Cu–Li alloy, Acta Mater. 75 (2014) 134-146.
[50] T. Dorin, F. De Geuser, W. Lefebvre, C. Sigli, A. Deschamps, Strengthening mechanisms of T1 precipitates and their influence on the plasticity of an Al–Cu–Li alloy, Materials Science and Engineering: A 605 (2014) 119-126.
[51] B.I. Rodgers, P.B. Prangnell, Quantification of the influence of increased pre-stretching on microstructure-strength relationships in the Al–Cu–Li alloy AA2195, Acta Mater. 108 (2016) 55-67.
[52] EFFECT OF A PRIOR STRETCH ON THE AGING RESPONSE OF AN AI-Cu-Li-Ag-Mg-Zr ALLOY, (1990).
[53] The role of plastic deformation on the competitive microstructural evolution and mechanical properties of a novel Al±Li±Cu±X alloy, (2001).
[54] J. Xu, Y. Deng, J. Chen, Y. Xie, X. Guo, Effect of ageing treatments on the precipitation behavior and mechanical properties of Al–Cu–Li alloys, Materials Science and Engineering: A 773 (2020).
[55] L. Zhan, J. Lin, T. Dean, A review of the development of creep age forming: Experimentation, modelling and applications, International Journal of Machine Tools and Manufacture 51(1) (2011) 1-17.
[56] Y. Xu, L. Zhan, W. Li, Effect of pre-strain on creep aging behavior of 2524 aluminum alloy, Journal of Alloys and Compounds 691 (2017) 564-571.
[57] E. Yucelen, I. Lazic, E.G.T. Bosch, Phase contrast scanning transmission electron microscopy imaging of light and heavy atoms at the limit of contrast and resolution, Sci Rep 8(1) (2018) 2676.
[58] H. Wang, L. Liu, J. Wang, C. Li, J. Hou, K. Zheng, The Development of iDPC-STEM and Its Application in Electron Beam Sensitive Materials, Molecules 27(12) (2022).
[59] Y.-C. Huang, C.-S. Tsao, C. Lin, Y.-C. Lai, S.-K. Wu, C.-H. Chen, Evolution of Guinier-Preston zones in cold-rolled Al0.2CoCrFeNi high-entropy alloy studied by synchrotron small-angle X-ray scattering, Materials Science and Engineering: A 769 (2020) 138526.

doi:10.6342/NTU202402902

[60] E. Broitman, Indentation Hardness Measurements at Macro-, Micro-, and Nanoscale: A Critical Overview, Tribology Letters 65(1) (2016) 23.

doi:10.6342/NTU202402902